Ocean Modelling 33 (2010) 70–86

Contents lists available at ScienceDirect

Ocean Modelling

journal homepage: www.elsevier.com/locate/ocemod

Non-uniform adaptive vertical grids for 3D numerical ocean models

Richard Hofmeister [a,*], Hans Burchard [a], Jean-Marie Beckers [b]

[a] Leibniz Institute for Baltic Sea Research Warnemünde, Dept. for Physical Oceanography and Instrumentation, Seestraße 15, D-18119 Rostock-Warnemünde, Germany
[b] University of Liège, MARE-GHER-AGO, Sart-Tilman B5, B-4000 Liège, Belgium

ARTICLE INFO

Article history:
Received 31 July 2009
Received in revised form 30 November 2009
Accepted 7 December 2009
Available online 24 December 2009

Keywords:
Adaptive non-uniform grid
3D ocean modelling
Numerical mixing

ABSTRACT

A new strategy for the vertical gridding in terrain-following 3D ocean models is presented here. The vertical grid adaptivity is partially given by a vertical diffusion equation for the vertical layer positions, with diffusivities being proportional to shear, stratification and distance from the boundaries. In the horizontal, the grid can be smoothed with respect to z-levels, grid layer slope and density. Lagrangian tendency of the grid movement is supported. The adaptive terrain-following grid can be set to be an Eulerian–Lagrangian grid, a hybrid σ–ρ or σ–z grid and combinations of these with great flexibility. With this, internal flow structures such as thermoclines can be well resolved and followed by the grid. A set of idealised examples is presented in the paper, which show that the introduced adaptive grid strategy reduces pressure gradient errors and numerical mixing significantly. The grid adaption strategy is easy to implement in various types of terrain-following ocean models. The idealised examples give evidence that the adaptive grids can improve realistic, long-term simulations of stratified seas while keeping the advantages of terrain-following coordinates.

1. Introduction

In Burchard and Beckers (2004) a strategy to create a vertical grid layer distribution that adapts the distribution of calculation points to the solution of a vertical 1D ocean model is presented. The purpose for that method was paving the way for extensions to 3D models where adaptations could be more beneficial than in a 1D case. In the present paper, we therefore generalise this approach to the more interesting 3D case, with the aim to provide some strategies to adapt the numerical grid vertically with keeping the horizontal distribution of coordinates unchanged. The reason for using adaptive grids in 3D models can be found in the analysis of the different advantages and drawbacks of the vertical coordinate systems classically used in 3D ocean models.

One can basically distinguish z-coordinate models (e.g., Modular Ocean Model, see Bryan, 1969), σ-coordinate models (e.g., Princeton Ocean Model, Blumberg and Mellor, 1987), or isopycnal models (e.g., Bleck and Smith, 1990; Bleck, 2002). For z-coordinates models grid lines are horizontal, for σ-coordinates they follow the topography and for isopycnal models they follow density surfaces. When comparing advantages and disadvantages of the different kind of models, it appears that the choice of a particular vertical coordinate system has some advantages in some occasions (and locations), but is not optimal in other locations or moments (see Griffies et al., 2000). Also sometimes, the optimal choice of the vertical coordinates would depend upon the characteristics of the circulation which may change in space and time. The presently optimal model should make use of z near surface, isopycnal coordinates in the interior and σ-coordinates at the bottom.

If one had a model in which different vertical coordinate systems could be used, one could more easily distinguish and separate the different contributions to changes in simulation results (as presented in Ezer (2005) for a downflow experiment). Such a hybrid coordinate model has already been introduced by Kasahara (1974) in the sense that a generalised vertical coordinate transformation was suggested for ocean models. The so called s-coordinate models or hybrid coordinate models (see Song and Haidvogel, 1994; Burchard and Petersen, 1997; Madec et al., 1998; Pietrzak et al., 2002) are now standard modelling tools. They allow vertical coordinates to be located in a completely arbitrary way and therefore allow to compare the effect of different choices of coordinate systems. However, presently generalised coordinates models do not yet consider the question how to dynamically change the coordinates in an optimal way so as to reduce the numerical discretisation errors. Errors that could be reduced include, e.g., errors in isopycnal diffusion discretisations (Beckers et al., 2000), pressure gradient errors (Deleersnijder and Ruddick, 1992), unsatisfactory representation of downslope flow of plumes (Beckmann and Döscher, 1997), numerical damping of internal waves (Stanev and Beckers, 1999) and numerical mixing in stratified basins (Rennau and Burchard, 2009).

* Corresponding author.
E-mail addresses: richard.hofmeister@io-warnemuende.de (R. Hofmeister), hans.burchard@io-warnemuende.de (H. Burchard), JM.Beckers@ulg.ac.be (J.-M. Beckers).

1463-5003/$ - see front matter © 2009 Elsevier Ltd. All rights reserved.
doi:10.1016/j.ocemod.2009.12.003

Such error reductions are generally not done dynamically, since hybrid models and more classic models are often used in an *a priori* way, where the coordinates are placed according to the modellers *a priori* knowledge of the processes to be properly resolved. This approach is certainly already advantageous compared to the classic models were such a free choice is not possible, but it does not use the possibility of adapting the coordinate positions during the calculation according to the modelling results themselves.[1]

Though standard in classic computational fluid dynamics (see Thompson et al., 1985; Liseikin, 1999) or atmospheric models (see Fiedler, 2002), the use of adaptive vertical grids in ocean models is rare. Exceptions are the use of grid adaptation by empirical functions to achieve boundary layer refinements in isopycnal models (see Dewar and McDougall, 2000; Holt and James, 2001; Bleck, 2002) or grid refinements on horizontally meshes (by adaptive nesting for example Blayo and Debreu, 1999). A general extension to the *s*-coordinate system has been suggested by Song and Hou (2006), who showed that hybrid coordinate systems allow for reducing discretisation errors without loosing the advantages of terrain-following coordinates. A hybridisation of different vertical grids with regard to global ocean modelling is used in the HYCOM model (Bleck, 2002; Halliwell, 2004; Chassignet et al., 2006) to allow the transition from an isopycnal grid for the deep ocean to a terrain-following grid in shallow waters and a near-*z*-level grid at the surface. Here our objective is to define and test strategies to generate dynamically adaptive vertical grids based on the simulation results themselves.

Some aspects of adaptive grids in meteorological modelling should be considered here. Behrens et al. (2000) used a semi-Lagrangian approach to move adaptive grid refinements in a meteorological model which allows to keep sharp structures in a moving grid even without increasing the total resolution of the model grid. For ocean modelling applications, Adcroft and Hallberg (2006) discuss the benefits and drawbacks of Lagrangian and Eulerian approaches and prefer an arbitrary Lagrangian–Eulerian method with a generally Lagrangian coordinate allowing for cross-coordinate flow. This is applied and tested for the adaptive grid method presented here.

The pressure gradient problem in σ or *s*-coordinate models (Mellor et al., 1994; Haney, 1991; Burchard and Petersen, 1997) is shown to be reduced by model techniques for non-isopycnal vertical coordinates. The vertically adapted grid generally has to deal with the calculation of horizontal gradients (Stelling and Van Kester, 1994) and the internal pressure gradient (Shchepetkin and McWilliams, 2003 and references therein).

Auclair et al. (2000) showed that an optimised grid placement (double σ-coordinate systems) and an optimised initial density field can significantly reduce truncation errors in ocean models at least for fixed grids. Also Song (1998) and Song and Wright (1998) argue that the truncation error in the pressure gradient calculation is minimised for optimal grid distributions. In meteorological modelling, grid adaption with respect to estimates of the truncation error for adaptive grids is advocated by Skamarock (1989). The vertical adaptive coordinate method is expected to optimise the vertical grid in an optimal way for calculating horizontal gradients. A near-isopycnal grid adaption would improve the representation of diffusive fluxes as discussed by Mellor and Blumberg (1985) and recently by Marchesiello et al. (2009). Advantages for mass transport modelling with a grid method adapting to vertical gradients of sediment are shown by Wai and Lu (1999) for modelling sediment transport. In their case, a Eulerian–Lagrangian technique was used for flat-bottom experiments. In general oceanic applications, it is needed to account for multiple state variables for the grid adaption (as the idea of Burchard and Beckers, 2004). Additionally, with coarser resolution and strongly varying topography, the grid could get distorted and needs strong horizontal filtering.

The paper is organised as follows: First the concept of general vertical coordinates is briefly reviewed with respect to the primitive equations (Section 2.1). Then, the grid adaptation strategies are derived (Section 2.2). Afterwards, the numerical methods for solving the dynamical equations in the framework of the moving grids are discussed (Section 2.3–2.8). In Section 3, the implementation concept into the used 3D model are described. These methods are then compared and investigated in detail for four different idealised model scenarios (Section 4). Finally, the results are summarised and discussed (Section 5).

2. Grid adaptation

2.1. The transformed model space

In order to increase the mathematical flexibility of a 3D ocean model, a general vertical coordinate transformation Γ following Kasahara (1974) and Deleersnijder and Ruddick (1992) is carried out which maps the physical space (t^*, x^*, y^*, z), with the vertical coordinate z pointing upwards, into a transformed space spanned by the coordinates (t, x, y, γ). The general vertical coordinate γ is assumed to be monotone with respect to z:

$$\gamma = \Gamma(t^*, x^*, y^*, z) \quad \Longleftrightarrow \quad z = z(t, x, y, \gamma) \tag{1}$$

The following coordinate change is thus used:

$$t^* = t, \quad x^* = x, \quad y^* = y, \quad z = z(t, x, y, \gamma) \tag{2}$$

with the Jacobian of the transformation being simply $\partial_\gamma z$. γ can be chosen for convenience to vary between -1 at the bottom and 0 at the surface.

One of the simplest coordinate transformation of this type is the so called σ-coordinate transformation

$$\gamma = \sigma = \frac{z - \eta}{D} \tag{3}$$

where η is the sea surface elevation (counted positive upwards from $z = 0$ at the reference surface) and $D = H + \eta$ is the total local depth (topographic depth H plus sea surface elevation).

The purpose of the present paper is to find some optimal way to define the function $z(t, x, y, \gamma)$. The adaptive coordinate must always and everywhere satisfy a non-vanishing Jacobian and total height conservation. Apart from these restrictions, the coordinate change is highly flexible and can therefore accommodate any desired treatment.

The dynamic equations in the physical space can then be integrated in the transformed, discretised space as presented in Burchard and Petersen (1997) or alternatively presented in Lander et al. (1994).

From here on, in order to simplify the numerical treatment, we try to find the non-uniform coordinate transformation $z(x, y, t, \sigma)$, where σ is uniformly distributed in $[-1, 0]$ corresponding directly to the discrete numerical vertical grid indices. From there the non-uniform γ distribution can be recovered by the definition

$$\gamma = \frac{z(\sigma) - \eta}{D} \tag{4}$$

The objective is to find the coordinate transformation

$$z = z(\sigma), \sigma \in [-1, 0] \tag{5}$$

which covers the domain $z \in [-H, \eta]$ in some optimal way.

[1] σ-coordinate models are of course adaptive grids in the sense that they follow sea surface elevation changes, and isopycnal models are also adaptive in the sense that they follow isopycnals. Here we refer to adaptive grids as to those which explicitly include a strategy to modify the vertical distributions of coordinate points by other means.

2.2. Optimisation technique

Optimisations for general vertical coordinates are starting with generalising the sigma distribution to be zoomed towards bottom and surface, also called s-grid, in order to optimise the near-surface and near-bottom resolution. In Fiedler (2002), a grid adaptation by an empirical function depending on mixed layer depth is presented. The grid transformation strategy here should generally optimise the resolution of vertical gradients based on *a priori* minimisations (approach advocated in Thompson et al. (1985) and follow up of Burchard and Beckers (2004)).

One possibility is minimising the cost function $\mathscr{I}_1$ defined by

$$\mathscr{I}_1 = \int_{-H}^{\eta} (\partial_\sigma f)\mathrm{d}z = \int_{-1}^{0} \partial_z f (\partial_\sigma z)^2 \mathrm{d}\sigma = \int_{-1}^{0} w_1 (\partial_\sigma z)^2 \mathrm{d}\sigma \tag{6}$$

for each individual water column in the model domain. Here the weight $w_1 = \partial_z f$ is obviously related to the rate of change of the function f or alternatively to the inverse length scale of the function variations.

Minimisation of (6) tries to find the coordinate change $z = z(\sigma)$ such that in the new coordinates, the gradients (with respect to the new coordinate) of f are uniform and small. The Euler–Lagrange equation for fixed end points $z(-1) = -H$ and $z(0) = \eta$ and assuming the weighting function depending on the normalised coordinates: $w_1 = w_1(\sigma)$ writes as

$$\partial_\sigma (w_1 \partial_\sigma z) = 0 \tag{7}$$

However, in practice the weighting will rather be dependant on physical space coordinates since ultimately this is what is of interest to the modeller. This can be handled by using Eq. (7) with a diffusion term for a discrete set of σ levels, but where w_1 must be updated at each change of z. Hence, (7) is essentially non-linear in that case. Another approach would be to accept the *a priori* dependence of w_1 on the physical space and to minimise instead

$$\mathscr{I}_2 = \int_{-1}^{0} w_1(z)(\partial_\sigma z)^2 \mathrm{d}\sigma \tag{8}$$

which lead to the same Euler–Lagrange equation as (7). It can easily be shown that this approach minimises the error when assuming piecewise constant functions for a discrete set of data points. Instead of solving the Euler–Lagrange equation exactly at each model timestep, we rather allow to move the grid towards this exact solution in a time-marching manner:

$$\partial_t z - \partial_\sigma \left(k^{grid} \partial_\sigma z \right) = 0 \tag{9}$$

with the grid-related diffusivity k^{grid} and $\sigma \in [-1, 0]$ and boundary conditions for z from $z(-1) = -H$ and $z(0) = \eta$.

According to Burchard and Beckers (2004), the grid diffusion coefficient k^{grid} (which has the physical unit s^{-1}) is calculated as

$$k^{grid} = \frac{D}{t_{grid}} \left(c_{N^2} K^{grid}_{N^2} + c_{S^2} K^{grid}_{S^2} + c_d K^{grid}_d + c_b K^{grid}_b \right) \tag{10}$$

with the stratification-related component

$$K^{grid}_{N^2} = \frac{\max(0, \partial_z \rho)}{\Delta\rho} \tag{11}$$

the shear-related component

$$K^{grid}_{S^2} = \frac{|\partial_z v|}{\Delta v} \tag{12}$$

the near-surface component

$$K^{grid}_d = \frac{1}{d + d_0} \tag{13}$$

and the background component

$$K^{grid}_b = \frac{1}{D} \tag{14}$$

Here, $\Delta\rho$ is a reference density difference and Δv a reference velocity difference. The grid diffusion timescale is denoted by t_{grid}. d is the distance from the surface, d_0 is a variable determining the intensity of the near-surface grid zooming and the coefficients c_X are the diffusion weights. For the discretised version see Burchard and Beckers (2004), where this approach is applied for a 1D water column model.

The optimisation technique to minimise the integral of layer-related, vertical gradients in the model grid as presented above is easy to implement in an ocean model. The minimisation distributes the state variables and the velocity fields onto the vertical grid to be represented uniformly. It is easy to ensure a positive Jacobian and boundary fitting, because it is a valid transformation in that sense. However, the minimisation does not give a direct link between adjacent verticals in the horizontal model grid. The only link is the continuity of the physical fields to which the adaption is done. The horizontal filter methods presented in the Sections 2.4–2.7 below will supply a link between neighbouring water columns. For application in ocean models, the choice of diffusion weights c_X is not unique and will depend on the objective of the model study.

2.3. Vertical discretisation

For the discretisation, the physical space is vertically divided into N layers. This is done by introducing internal surfaces z_k, $k = 1, \ldots, N-1$ which do not intersect, each depending on the horizontal position (x, y) and time t:

$$\begin{aligned} -H(x,y) = z_0(x,y) < z_1(x,y,t) < \ldots < z_{N-1}(x,y,t) \\ < z_N(x,y,t) = \eta(x,y,t) \end{aligned} \tag{15}$$

with the local layer depths

$$h_k = z_k - z_{k-1} \tag{16}$$

for $1 \leqslant k \leqslant N$, the local bottom coordinate, $H(x, y)$, and the sea surface elevation, $\eta(x, y, t)$. The objective of the grid adaption is to find a distribution of the vertical location of interfaces z_k so as to place a given number of discrete grid points in an optimal way in terms of the specified optimisation parameters. This is leading to the height of the grid layers of $h_k = z_k - z_{k-1}$ with $\sum_k h_k = H + \eta$ if the grid is formed correctly with $z_0 = -H, z_N = \eta$ and $z_k > z_{k-1}$.

The horizontal transports are calculated from the hydrostatic Reynolds-averaged Navier–Stokes equations in the physical model space. The vertical velocity equation reduces for hydrostatic flow to the hydrostatic balance,

$$\partial_z p = -g\rho \tag{17}$$

such that for incompressible flow the vertical velocity w is calculated by means of vertically integrating the incompressibility condition

$$\partial_x u + \partial_y v + \partial_z w = 0 \tag{18}$$

where p is the pressure, g the gravitational acceleration and (u, v, w) are the components of the velocity vector. The discretisation of (18) is of the following form:

$$\bar{w}_k = \bar{w}_{k-1} - \partial_t h_k - \partial_x p_k - \partial_y q_k \tag{19}$$

with the grid-related vertical velocity

$$\bar{w}_k = \partial_t z_k - u|_{z_k} \partial_x z_k - v|_{z_k} \partial_y z_k \tag{20}$$

and the layer-integrated transports

$$p_k = \int_{z_{k-1}}^{z_k} u\,dz, \quad q_k = \int_{z_{k-1}}^{z_k} v\,dz \tag{21}$$

see Burchard and Petersen (1997) for details.

2.4. Horizontal filtering of interface positions

The independently adapted vertical coordinates can be homogenised horizontally by having similar vertical positions for the same levels on σ. However, the truncation error in the calculation of horizontal gradients in a horizontally non-aligned vertical coordinate system is indicated to be small for a small value of

$$A_{hc} = \frac{|\partial_x z_k|}{h_k/\Delta x} \tag{22}$$

where $A_{hc} \geqslant 1$ if the hydrostatic consistency is violated and extrapolations are expected. In our case with arbitrary small h_k, the potential errors can be reduced by a horizontal diffusion of the vertical position for each discrete level on the numerical grid σ. The filtering can be defined as

$$\partial_t z_k = \partial_x(\mathscr{A}_i \partial_x z_k) + \partial_y\left(\mathscr{A}_i \partial_y z_k\right) \tag{23}$$

where x and y are the spatial coordinates of the numerical grid and the diffusivity $\mathscr{A}_i$ scales with $\alpha_{hor}\frac{\Delta x^2}{4\Delta t_f}$. Δt_f is a timescale for the horizontal filtering, which is the baroclinic timestep in the shown experiments, and α_{hor} is a number between [0,1] and defines the strength of the horizontal filtering of interface positions.

The horizontal filtering of interface positions is a control on the horizontal regularity of the grid and it is easy to implement. For the resulting 2D elliptic equation, no extrema may exist. If a local extrema exist in a specific vertical, the filtering in the whole model domain may result in a non-unique coordinate change. The filtering may also lead to negative Jacobians and interface depths below topography. Hence an enforcing of well-defined grid is required afterwards (see Section 2.8).

At the lateral boundaries, Dirichlet or Neumann-type conditions could be applied.

2.5. Advection of z, Lagrangian approach

The incompressibility condition (19) can be rewritten as

$$\partial_t h_k + \partial_x p_k + \partial_y q_k = \bar{w}_{k-1} - \bar{w}_k \tag{24}$$

The transformed vertical velocity $\bar{w}$ relative to the moving grid is defined such that fluxes across coordinate surfaces are zero if this velocity is zero. For pure Lagrangian-type models, $\bar{w} = 0$ is defined. Normally, Eq. (24) is used to diagnose vertical velocities from prescribed changes in the grid and divergence of the velocity field as presented in the model description for the model used here.

But it can also be used to enforce Lagrangian movements of the grid by solving the equation for h_k imposing zero relative vertical velocity:

$$\partial_t h_k = -\partial_x p_k - \partial_y q_k \tag{25}$$

will give a first guess for new positions $\tilde{h}_k^{n+1}$ from which the new values can be calculated by any further re-gridding strategy. The Lagrangian-type guess for the new layer heights is

$$\tilde{h}_k^{n+1} = h_k^n - \alpha_{lag}\Delta t(\partial_x p_k + \partial_y q_k) \tag{26}$$

where the upper indices denote the time step numbers. For values $\alpha_{lag} = 1$, the vertical discretisation change (26) is fully Lagrangian and values $\alpha_{lag} < 1$ are introducing a Lagrangian tendency only. The Lagrangian approach decreases the grid-related vertical transports and thus the numerical mixing resulting from vertical advection of vertical tracer and momentum gradients. However, the grid-related vertical velocities are calculated after the grid adaption using Eq. (19).

The Lagrangian tendency minimises vertical advection and associated numerical mixing since strong vertical gradients moving with the vertical flow velocity are typical in oceanic applications. It is easy to implement if the grid adaption is placed correctly into the model loop. Nevertheless, the Lagrangian tendency may lead to invalid grids and layer interfaces below topography or above sea level. If an initial distribution of layers is defined, a pure Lagrangian advection of layers cannot control the grid regularity, especially not, if open boundaries are included in the model domain.

2.6. Horizontal filtering of layer thicknesses

Violating the hydrostatic consistency in the model grid discretisation indicates possible truncation errors, which feed into the calculation of the internal pressure gradient. Song (1998) estimates the error for the pressure gradient calculation over a vertical extent of a single cell scales with $\delta_x(\delta_\sigma z)$ (in our notation: $\delta_x h_k$) for a buoyancy field which can be represented by second-order polynomials in the vertical.

Beside that, the magnitude of the pressure gradient error is depending on the pressure gradient formulation (PGF) itself. Higher order terms for the representation of the buoyancy field will result in higher order terms for the error in the PGF. According to Song (1998), the discretisation error disappears for

$$\delta_x h_k = 0 \tag{27}$$

a condition, which can be approached by applying a horizontal diffusion of layer thickness. The diffusion of layer thickness writes as

$$\partial_t h_k = \mathscr{A}_h\left(\partial_{xx} + \partial_{yy}\right) h_k \tag{28}$$

where $\mathscr{A}_h$ scales with $\alpha_{dif}\frac{\Delta x^2}{4\Delta t_f}$ and α_{dif} is a number between [0,1] and defines the strength of the horizontal filtering of layer thicknesses.

Next to the reduction of PGF errors, the horizontal diffusion of layer height is an additional control for the horizontal regularity of the grid. Drastical changes between adjacent water columns are smoothed. The iterative process of the vertical optimisation technique and the horizontal filtering of layer thicknesses tends to create "iso-gradient" layers, which are locally similar to isopycnal layers for small isopycnal slopes and distant to the bottom and the surface.

The horizontal filtering of layer thicknesses can have the same effect as the horizontal filtering of layer heights for special scenarios. For a horizontally varying, vertical optimisation effect or bathymetry, both filters will act differently.

However, in addition to the diffusion of layer height h, the conservation of total depth may be violated (similar problems as with the horizontal bolus velocity in isopycnal models (see Gent and McWilliams, 1990)). The conservation of total depth has to be enforced separately as suggested in Section 2.8. Thus the effect of minimising the pressure gradient error is limited. At least in a pure σ-coordinate grid, the effect of horizontal diffusion of layer height is compensated by the depth conservation.

2.7. Isopycnal tendency

The objective for this aspect of the grid adaption strategy is to place z_k to be on user-defined ρ surfaces. Special treatments are needed at the bottom, the surface and for interleaving layers in pure isopycnal models, when isopycnals disappear or new layers have to be added. Therefore, the objective is move in time the point from z_k^n into a position z_k^{n+1} where the density has a given value ρ_k^*. This can be achieved by observing that

$$\rho(z^{n+1}) \sim \rho(z^n) + (z^{n+1} - z^n)\partial_z \rho \tag{29}$$

So that the best guess for the update would be

$$z_k^{n+1} = z_k^n + \frac{\rho_k^* - \rho(z^n)}{\partial_z \rho} \tag{30}$$

meaning that one can add the following tendency term

$$z_k^{n+1} = z_k^n + \alpha_{iso} \frac{\rho_k^* - \rho(z^n)}{\partial_z \rho} \quad \alpha < 1 \tag{31}$$

where $\alpha_{iso} = 1$ is strong isopycnal tendency and $\alpha_{iso} = 0$ is no isopycnal tendency.

ρ_k^*, the target isopycnal value for level k can be prescribed *a priori* like in isopycnal models, but it could be more flexible to let the model calculate the target densities from the density distribution itself. This can be achieved iteratively by assigning to ρ_k^* a mean value of all ρ_k from surrounding water columns. The stencil for the averaging can be large if some basin scale "isopycnals" are thought. Averaging only over sub-basin scales also allows different "isopycnals" to be used in physically different regimes. In Section 3 an example method for calculating the ρ_k^* values is given as used for the examples.

Of course, instead of pushing given discrete levels to prescribed isopycnal levels, one could also attract them in a similar way to prescribed z level, oxygen values or any other *a priori* distribution. A pure grid adaption towards prescribed z levels will create a hybrid grid between σ-coordinate and z-level grids.

The advantage of using such an isopycnal tendency (coupled possibly with the Lagrangian tendency) compared to purely isopycnal models is that the grid does not stick on preserving certain density values. Hence, the well tested model techniques for calculating the vertical mixing and handling the non-linear effects of the equation of state (such as cabbeling) can kept the same. Furthermore, if the physical situation precludes efficient use of purely isopycnal models (for example during deep water formations), the adaptive grid method simply will move grid points in a non-isopycnal way.

The method also could allow to prescribe different isopycnal levels (to which grid points are attracted) in different basins, with transition zones. Again, the numerical grid, since it is absolutely arbitrary, does not need to adapt physical parameterisations as they are already included in the primitive equation model. The advantage of trying to follow isopycnals simply lies in the fact that if the physical processes are isopycnal, then the numerical grid allows a better representation of those processes as they are aligned with the grid.

Again, the isopycnal tendency may lead to invalid grids and interface depths below topography so that total depth conservation has to be ensured. If there is noise in the isopycnal depths, it will be transferred to the numerical grid by the isopycnal tendency, which may have impacts on the horizontal resolution of the flow field.

2.8. Enforcing well-defined grids

Working with the layer heights h_k allows easy diffusion of h, but it may lead to a "conservation" problem of the local total depth for the adapted grid. Working with the interface positions z_k might result in negative layer heights. For a well-defined grid, it has to ensured that $z_0 = -H$ and $z_N = \eta$. Additionally it has also to be enforced that $z_{k+1} > z_k$.

If the approach is based on layer thickness tapering or horizontal diffusion of z-levels, one must always include the constraint

$$\sum_k h_k = H + \eta \tag{32}$$

and $h_k > 0$. We aim for a single step correction (or at least a finite (known and proportional to N) number of steps) in order to control the computing cost.

The implementation is to always check for positive layer heights and enforce the layer heights to be larger than a specified minimum depth. Finally, the adapted, uncorrected grid $\tilde{h}_k$ is corrected to match the local depth by

$$h_k = \left(\alpha_k \frac{H + \eta}{\sum \alpha_k \tilde{h}_k}\right) \tilde{h}_k \tag{33}$$

where the correction weights α_k can be also used to concentrate even more levels where needed (see Liseikin, 1999). Here we use $\alpha_k = 1$ to apply a global compression/expansion to fit the total depth.

3. Implementation

3.1. 3D model specifications

The grid adaptation, which is introduced here, is implemented into the GETM (General Estuarine Transport Model, Burchard and Bolding, 2002; Burchard et al., 2004, see also www.getm.eu) model which is a fully baroclinic model based on the primitive equations with turbulent closure schemes from GOTM (General Ocean Turbulence Model, Umlauf et al., 2005; Umlauf and Burchard, 2005, see also www.gotm.net). Various GETM applications (Burchard et al., 2004, 2008, 2009; Stanev et al., 2003; Banas and Hickey, 2005; Umlauf and Lemmin, 2005; Staneva et al., 2009; Hofmeister et al., 2009) show that the model is able to reproduce observed physical regimes in estuaries, coastal seas and lakes. The model numerics contain high-order advection schemes for momentum and tracer advection (Pietrzak, 1998; Burchard and Bolding, 2002) and various pressure gradient formulations (as presented in Shchepetkin and McWilliams (2003)). In the vertical, a flexible, general vertical discretisation for terrain and surface following coordinates (see Burchard and Bolding, 2002) are implemented. The model has a free surface and a mode-splitting implemented, which allows to have a smaller timestep for the barotropic mode as for baroclinic mode. Both modes are two-way coupled such that the vertically integrated horizontal transports are consistent (see Burchard and Bolding (2002) for details). The vertical grid calculation (including the grid adaption) is part of the baroclinic mode. Regarding the layer distribution, there are three options for the initialisation of a model run:

(a) Starting with predefined distributions for temperature and salinity without any velocities, and a sigma-type layer distribution, the grid adaption is expected to take place during the model run.
(b) Starting with predefined distributions for temperature and salinity without any velocities and pre-adaption of the grid to the density distribution and the bathymetry. During the pre-adaption process, only vertical transport through the layer interfaces is allowed. After the pre-adaption, a balance between adaption to stratification and bathymetry should be approached, in order to avoid a strongly moving grid at the beginning of the simulation. The initial temperature and salinity fields are re-interpolated onto the pre-adapted model grid afterwards.
(c) Starting in hotstart mode, which continues an existing simulation. The information, which is needed at the beginning of a simulation loop is read from a file during initialisation.

3.2. Implementation of the grid adaption in the model loop

The grid adaption is part of the baroclinic mode calculation in the main model loop. The main order in the loop of the baroclinic mode is

1. Updating the horizontal transports;
2. Updating the grid (which is the grid adaption in case of adaptive grids) and the grid-related vertical velocities.
   (a) The pseudo-Lagrangian adaption (Eq. (26) in Section 2.5) and the horizontal diffusion of layer height (Eq. (28) in Section 2.6) and additionally an enforcing of well behaved grid is called (see Section 2.8). The horizontal diffusion of layer heights is not activated between land and water cells and outside the model domain at the open boundaries.
   (b) The vertical refinement of the grid by horizontal filtering of interface positions (Eq. (23) in Section 2.4) and the isopycnal tendency (Eq. (31) in Section 2.7): The horizontal filtering of interface positions is switched off for thin layers (if the layer height less than the specified minimum depth) and between land and water cells. The distance of interface movement by the isopycnal tendency is limited to be less or equal the layer height in order to avoid pathologic grids when strong along-layer gradients are existing (e.g., near a plume front or steep slopes).The isopycnal tendency is calculating its reference densities by averaging over a given horizontal stencil of 5×5 grid points within the specific model layer:

$$\rho^*_{i,j,k} = \frac{1}{\sum_{i',j'=i-2,j-2}^{i+2,j+2} m_{i',j'}} \sum_{i',j'=i-2,j-2}^{i+2,j+2} m_{i',j'} \cdot \rho_{i',j',k} \tag{34}$$

   where i, j, k are the grid cell indices in the 3D model grid and m is a land mask with $m = 0$ for land cells and $m = 1$ for water cells. Again the enforcing of a well behaved grid is called.
   (c) The grid adaption to stratification, shear and distance to bottom and surface (Eq. (9) in Section 2.2). A background adaption towards an equally spaced vertical grid is calculated for the sum of the four related tendencies equalling one. The different tendencies could be combined locally weighted, depending on depth, velocity, sub-basin averaged stratification for example. In our case, the weights are specified constant in time and space. The vertical diffusion in the grid adaption is calculated implicitly.
   (d) The grid-related vertical velocities are calculated from Eq. (19).
3. Evaluating the turbulent mixing quantities;
4. Updating temperature, salinity and finally density distributions.

For the final moving of data when grid points have been adapted, a high-order advection scheme is needed (Iselin et al., 2002). The updated distribution of tracers and transports is calculated by means of the chosen advection scheme based on the grid-related vertical velocities, calculated after the grid handling in the model loop. Thus, a specific remapping of tracer and velocity fields as presented in White and Adcroft (2008) is not necessary here. In addition, with the present approach tracer conservation is ensured by the advection scheme. It should be noted that due to the tracer re-distribution by the high-order advection schemes, filtered gridding is not leading to filtered tracer distributions.

The grid adaptation must be done just before mass conservation in the model loop, which is assured in our model by the calculation of the grid-related vertical velocity.

The different parameters of the grid adaption are listed as follows:

α_{hor}	factor for horizontal filter of interface positions
α_{lag}	factor for Lagrangian tendency (see (26))
α_{dif}	factor for horizontal filter of layer heights h_k
α_{iso}	factor for isopycnal tendency (see (31))
c_{N^2}	diffusion weight related to stratification
c_{S^2}	diffusion weight related to shear
c_d	diffusion weight related to distance from surfaces
d_{surf}	norm for distance related to c_d
d_{min}	minimum height for enforcing well-defined grids
t_{grid}	grid adaption timescale

The diffusion weights from (10) should add up to $1 = c_{N^2} + c_{S^2} + c_d + c_b$. Hence, the diffusion weight related to the background σ-layer distribution is calculated accordingly and is excluded from the list of free parameters. Typical sets of these grid adaption parameters are given in the examples, discussed in the next section. It is possible that linking of parameters will be practical in realistic studies, for example linking the Lagrangian and isopycnal tendency in order to get isopycnal-type coordinates. Also α_{dif} might be linked to the diffusion weights and the minimum layer height in order to force the horizontal smoothing, when potentially distorted grids are expected.

The computational overhead by the grid adaption is mostly determined by an additional call to the implicit solver for the vertical grid diffusion and the calculation of the running mean of the density for the isopycnal tendency. Therefore, the calculation of the running mean of the density is skipped if α_{iso} is zero.

4. Examples

The examples in the following will investigate the performance of the grid adaption in terms of numerical mixing (internal seiche (Section 4.1) and multi-basin overflow (Section 4.2) examples) and in terms of pressure gradient errors for experiments with an oceanic seamount (Section 4.3). In a coastal upwelling experiment (Section 4.4), the grid adaption is applied to a more realistic scenario. In all of the examples, the best-practice model techniques of GETM are used. A third-order, monotonic TVD scheme is used for advection of density and velocity and in general a high-order internal pressure gradient scheme (Shchepetkin and McWilliams, 2003) is adopted.

Mixing is quantified here as the tracer variance decay, which can be evaluated for the numerically and physically induced mixing as presented by Burchard and Rennau (2008). The tracer variance decay by physical mixing D^{phys} is estimated by the decay term in the budget equation for the square of the mean tracer s due to turbulent diffusion

$$D^{phys} = 2K_v(\partial_z s)^2 \tag{35}$$

where K_v is the vertical component of the turbulent diffusivity. Contributions from the horizontal diffusivity are neglected, because it is switched off in the following examples. D^{phys} can be directly compared to the tracer variance decay due to numerical mixing, which can be calculated by the difference between the advected amount of the squared tracer and the squared amount of the advected tracer divided by the time step Δt (see Burchard and Rennau, 2008). The tracer variance decay due to numerical mixing D^{num} for a certain model grid cell i at a certain time step number $n+1$ writes as

$$D_i^{num} = \frac{A\left\{\left(s_i^n\right)^2\right\}_i - \left(A\left\{s_i^n\right\}_i\right)^2}{\Delta t} = \frac{A\left\{\left(s_i^n\right)^2\right\}_i - \left(s_i^{n+1}\right)^2}{\Delta t} \tag{36}$$

where $A\{\ldots\}_i$ is the tracer concentration resulting from a pure advection step and Δt is the time step. The tracer concentration s_i^{n+1} is obtained after the advection step in cell number i. Eq. (36) can be integrated in the discrete model space with grid cell heights h_i^{n+1} as

$$\Delta t \sum_i h_i^{n+1} D_i^{num} = \sum_i h_i^{n+1} A\left\{\left(s_i^n\right)^2\right\}_i - \sum_i h_i^{n+1}\left(s_i^{n+1}\right)^2 \tag{37}$$

Since the advection schemes used here are conservative, for closed domains without boundary fluxes, (37) can be written as

$$\Delta t \sum_i h_i^{n+1} D_i^{num} = \sum_i h_i^{n}\left(s_i^{n}\right)^2 - \sum_i h_i^{n+1}\left(s_i^{n+1}\right)^2 \tag{38}$$

Hence, the difference of the tracer variance in a closed domain before and after the advection step is given by the domain-wide integral of the value D_i^{num}.

Riemenscheider and Legg (2007) showed that in basin-scale overflow simulations the expected mixing of tracers is covered exhaustively by the numerical mixing. Hence, the simulated tracer mixing was depending on the model resolution, which is unsatisfactory for a physical description of the mixing processes. The numerical mixing is needed for the monotonicity of the advection scheme. It has to be reduced as much as possible within this requirement by the model numerics in order to get a physically based description of the mixing by a turbulence model. It is expected here that the physical mixing parameters in the model are represented in a quantitatively realistic way by properly implemented turbulence closure models (see, e.g., the 1D model-observation comparison studies by Burchard et al. (2002), Simpson et al. (2002), Arneborg et al. (2007), Souza et al. (2008), Peters and Baumert (2007), or the 3D model study by Ilicak et al. (2008)). The physical and numerical mixing contributions always compete in reducing the tracer variance in the model domain. It is thus expected that a reduced numerical mixing could increase the amount of physical mixing with the same turbulent diffusivity but acting on stronger gradients.

4.1. Internal seiche

This two-layer flow scenario will demonstrate that the Lagrangian approach indeed allows to move grid points passively with the vertical velocity field. It will further be shown that grids which are directly adapted to the changing vertical stratification substantially reduce numerical mixing and perform similarly to Lagrangian grids. We will further show that in contrast to these adaptive grids a fixed grid will cause strong numerical diffusion with the effect that the seiche period is overestimated.

For this test case which is based on a 2D closed flat bottom domain with a length of $L = 64$ km and a mean depth of $H = 20$ m, friction and mixing are neglected in order to allow for an analytical solution. The two layers have a density difference of $\Delta\rho = 3.9\ \mathrm{kg\ m^{-3}}$. The initial interface between the two layers is located at

$$z^* = -\frac{H}{2}\left(1 - \epsilon \sin\left(\pi\frac{x}{L}\right)\right) \tag{39}$$

for $x \in \left[-\frac{1}{2}L, \frac{1}{2}L\right]$, where $x = 0$ is the basin centre. The relative amplitude ϵ, is also a measure for the non-linearity of the scenario. Initial velocities are zero, the initial sea surface elevation is set to

$$\eta = -\frac{g'}{g}\frac{H}{4}\epsilon \sin\left(\pi\frac{x}{L}\right) \tag{40}$$

with the reduced gravitational acceleration

$$g' = \frac{\Delta\rho}{\rho_0} g \tag{41}$$

In this case, the linearised solution from LeBlond and Mysak (1978) for small density differences can be decomposed in the barotropic and baroclinic modes. Hence the solution for the interface position is

$$z^* = -\frac{H}{2}\left(1 - \epsilon\cos(\omega t)\sin\left(\pi\frac{x}{L}\right)\right) \tag{42}$$

and

$$\eta = -\frac{g'}{g}\frac{H}{4}\epsilon \sin\left(\pi\frac{x}{L}\right)\cos(\omega t) \tag{43}$$

for the sea surface elevation η with the frequency

$$\omega = \frac{1}{2}\sqrt{g'H}\,\frac{\pi}{L} \tag{44}$$

The analytical solution for $\epsilon \to 0$ for the upper layer velocity u^+ and the lower layer velocity u^- is

$$u^+ = -u^- = \frac{\epsilon}{2}\sqrt{g'H}\sin(\omega t)\cos\left(\pi\frac{x}{L}\right) \tag{45}$$

The discretisation for this scenario is carried out with a horizontal resolution of $\Delta x = 500$ m, a barotropic timestep of 15 s, a baroclinic timestep of 150 s and $N = 20$ vertical layers. In order to avoid interpolation of the initial density distribution into the numerical grid, the initial vertical grid is constructed such that the middle layer is aligned with the density interface and the remaining layers are distributed with equidistant spacing between the bottom and the interface and the interface and the surface, respectively:

$$h_k = \begin{cases} \frac{-z^*+\eta}{\frac{1}{2}N}, & k = \frac{1}{2}N+1,\ldots,N \\ \frac{H+z^*}{\frac{1}{2}N}, & k = 1,\ldots,\frac{1}{2}N \end{cases} \tag{46}$$

with the density jump between $k = \frac{1}{2}N$ and $k = \frac{1}{2}N + 1$.

In the upper panel of Fig. 1 the solutions for the normalised lower layer velocity u^- at $x = 0$ for four different grid types and a non-linearity of $\epsilon = 0.2$ are compared to the analytical linear solution (45): the fully Lagrangian grid, the adaptation to stratification, the adaption to shear and the grid fixed to the initial grid with fitting to the changing water depth, only. In order to enable a fully Lagrangian grid, the background diffusivity c_b is exceptionally set to zero. The parameters for the grid adaptions are listed in Table 1, unmentioned parameters equal zero for all experiments.

It is clearly seen that the Lagrangian grid and the adaptive grids based on vertical optimisation are close to each others and also close to the linear analytical solution. In contrast to this, the solution with the fixed grid strongly deviates from the other solutions, both, in period and amplitude.

Fig. 2 shows layer and density distribution for the fixed grid and the grid adapted to stratification after half of a period of oscillation. It can be clearly seen that the result with the fixed grid is highly diffusive and the solution thus is inaccurate.

In order to prove that the normalised Lagrangian solution (as well as the adaptive-grid solutions) converges towards the normalised linear analytical solution for $\epsilon \to 0$, simulation results for $\epsilon = 0.1$ are shown for the adaptive grids and the fixed grid in the lower panel of Fig. 1. The solutions for the adaptive grids are indeed close to the analytical solution again, whereas the fixed grid solution strongly deviates from it.

4.2. Multi-basin overflow

A second example showing a reduction of numerical mixing by the adaptive vertical coordinates is a marginal sea overflow scenario as studied intensively already by Burchard and Rennau (2008) in terms of numerical mixing. The bathymetry is a simplified transect through the Baltic Sea, following the major inflow

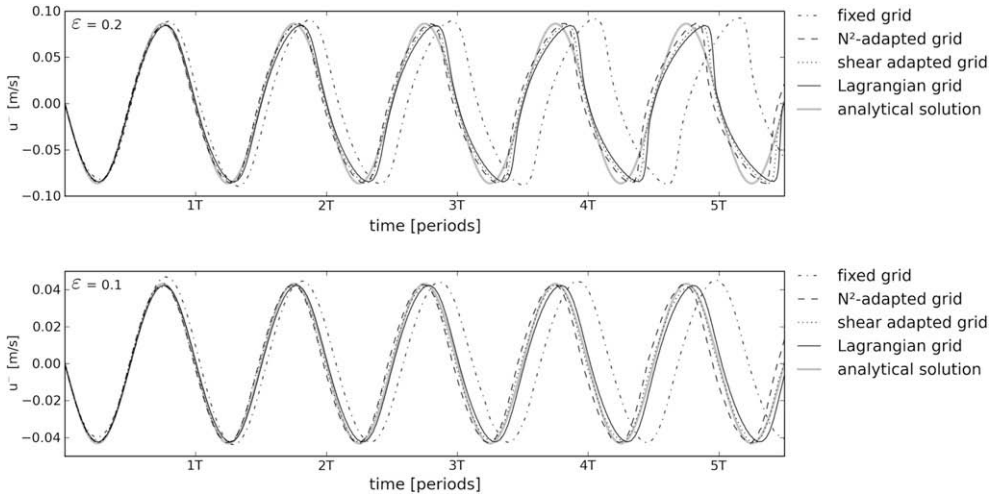

Fig. 1. The lower layer velocity in the seiche experiment for four different grid types compared to the analytical solution from (45). The upper panel results are for a non-linearity of $\varepsilon = 0.2$ and the lower panel for a non-linearity of $\varepsilon = 0.1$.

Table 1
Parameters for the grid adaptions in the internal seiche experiments.

Grid	α_{lag}	α_{dif}	c_{N^2}	c_{S^2}	c_b	d_{min} (m)	t_{grid} (h)
Fully Lagrangian	1.0	0.0	0.0	0.0	0.0	0.1	1
Adaption to stratification	0.0	0.5	0.5	0.0	0.5	0.1	1
Adaption to shear	0.0	0.5	0.0	0.5	0.5	0.1	1

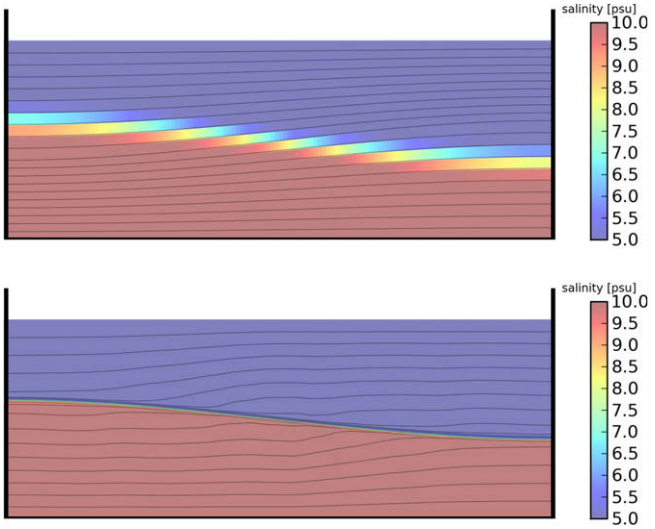

Fig. 2. The salinity distribution for the fixed grid (upper panel) and the adaptive grid (lower panel) after half of a seiching period. The black lines denote the positions of the layer interfaces.

events discussed in, e.g., Feistel et al. (2006). The model domain (see Fig. 3) has a horizontal resolution of 2100 m, 40 vertical levels and is closed at both sides of the horizontal axis. The density field does only depend on salinity here and a lock-exchange type inflow is generated by initialising the salinity to be 25 psu for $x \leqslant 125$ km and 8 psu elsewhere. The induced horizontal pressure gradient forces a dense bottom current over the sills into the subsequent basins (according to the Baltic Sea from left to right: Arkona Sea, Bornholm Sea, Stolpe Furrow, Gotland Deep). Meteorological forcing and earth rotation are neglected in the simulation. Fig. 3 shows the salinity distribution after 20 days, when the basins are partially filled and the residual part of the inflow has to propagate above the already denser water in the basins.

The adaptive coordinates configured by the parameters in Table 2 help here to reduce the vertical advection through the layer interfaces by moving the layer interfaces with stratification. After the basins are partially filled, the overflow will detach from the sea bed and will entrude into its density horizon. The vertical grid adaption aligns the coordinates along the isopycnals, thus reducing the density gradient in flow direction.

In Fig. 4 the salinity, horizontal velocity, numerical mixing and physical mixing is shown for the outflow from the first basin (denoted in Fig. 3) in the simulation for σ-coordinates. The overflow is resolved with few vertical layers and numerical mixing occurs within the overflow. The pycnocline is distorted in the basins due to the bottom-following coordinates and the coarse horizontal resolution. The numerical mixing is highest when the overflow reaches the denser water in the deeper basin, due to relatively large horizontal density gradients and horizontal as well as vertical

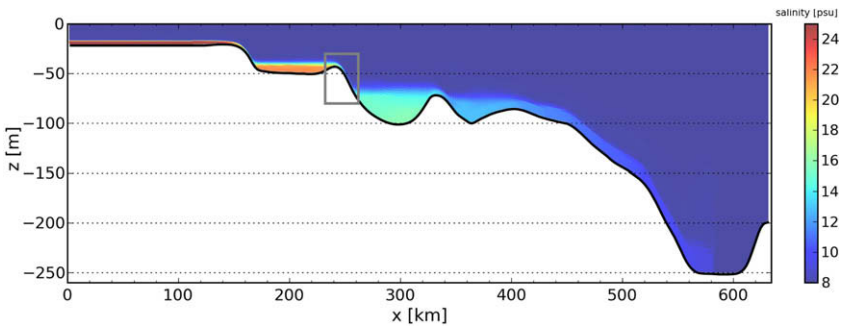

Fig. 3. Salinity distribution for the 2D overflow experiment after 20 days of simulation. The region within the gray rectangle will be investigated in more detail in Figs. 4 and 5.

Table 2
Parameters for the grid adaption in the multi-basin overflow experiment.

α_{hor}	α_{lag}	α_{dif}	α_{iso}	c_{N^2}	c_{S^2}	c_d	d_{surf} (m)	d_{min} (m)	t_{grid} (h)
0.1	0.1	0.3	0.1	0.2	0.0	0.3	20	0.1	3

velocities. Significant reduction of numerical mixing is obtained in the simulation with adaption to stratification and application of all horizontal filters. The important, horizontal filters are the isopycnal tendency and a small Lagrangian tendency here. The Lagrangian tendency reduces the vertical advection through the layer interfaces directly, the adaption to stratification will keep the resolution at the pycnocline and the isopycnal tendency aligns the coordinates along the pycnocline in the horizontal. Fig. 5 shows a better representation of the density field and less numerical mixing in the overflow for the adaptive grid compared to the σ-grid. The high, numerical mixing at the position where the overflow plunges into the denser water in the deeper basin still occurs as a result of the vertical and horizontal advection in the already adapted grid. However, the numerical mixing at the slope reduces to a thin band of diffusive and anti-diffusive fluxes due to the slightly moving density interface.

Burchard and Rennau (2008) evaluated the vertical integral of the tracer variance decay for the physical and the numerical mixing as measure for the influence of model numerics onto the simulation results. Fig. 6 shows that adaptive coordinates reduce the amount of numerical mixing in the simulation by more than 45%. The physical mixing is slightly increased because of stronger, remaining density gradients with decreased numerical mixing. In the simulation with the adaptive vertical coordinates, the largest contribution to the overall mixing is shifted from numerically induced to physically induced mixing.

4.3. Seamount test case

The seamount problem (similar to Beckmann and Haidvogel, 1993) is the standard scenario for evaluating pressure gradient errors in non-aligned vertical coordinate systems (Chu and Fan, 1997; Mellor et al., 1998; Song and Wright, 1998; Shchepetkin and McWilliams, 2003). It is a simulation of a horizontally homogeneous stratification in a 5000 m deep ocean with a Gaussian-shaped seamount of 4500 m height (see Fig. 7 for an overview). The domain of 66×66 equidistant grid points and a horizontal resolution of 8 km is closed at the horizontal boundaries here and no external forcing is applied. The density variations are only depending on temperature variations here and the initial temperature profile is given by

$$T(z) = 5 + 15e^{z/\delta}, \quad -H \leqslant z \leqslant 0 \tag{47}$$

where $\delta = 1000$ m and $H = 5000$ m.

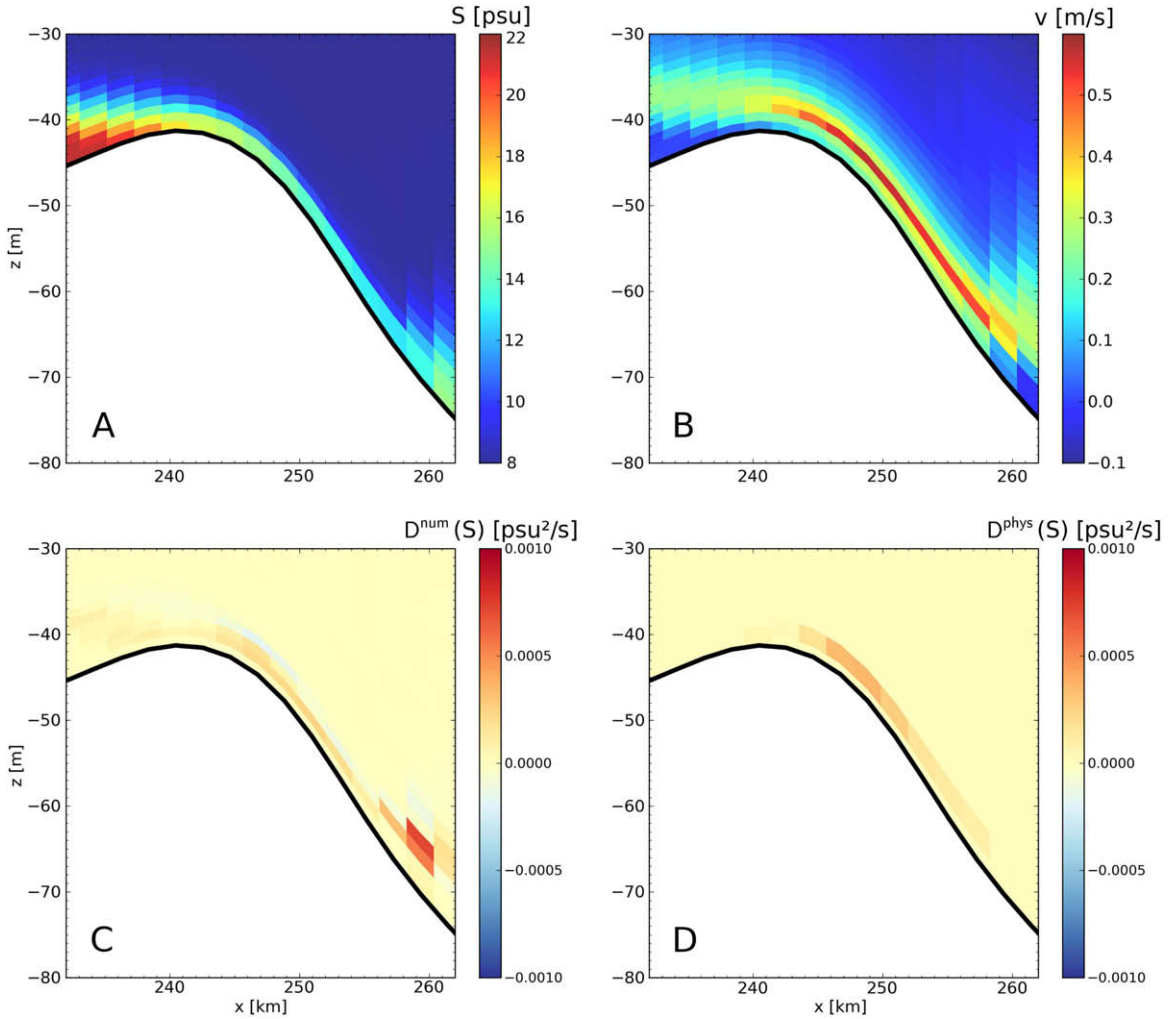

Fig. 4. Analysis of effective mixing processed inside the small subdomain in Fig. 3 for the simulation with a fixed σ-grid. (A): salinity, (B): horizontal velocity, (C): numerical salinity variance decay, (D): physical variance decay. The physical tracer variance decay has been interpolated onto the tracer grid, given as coloured polygons.

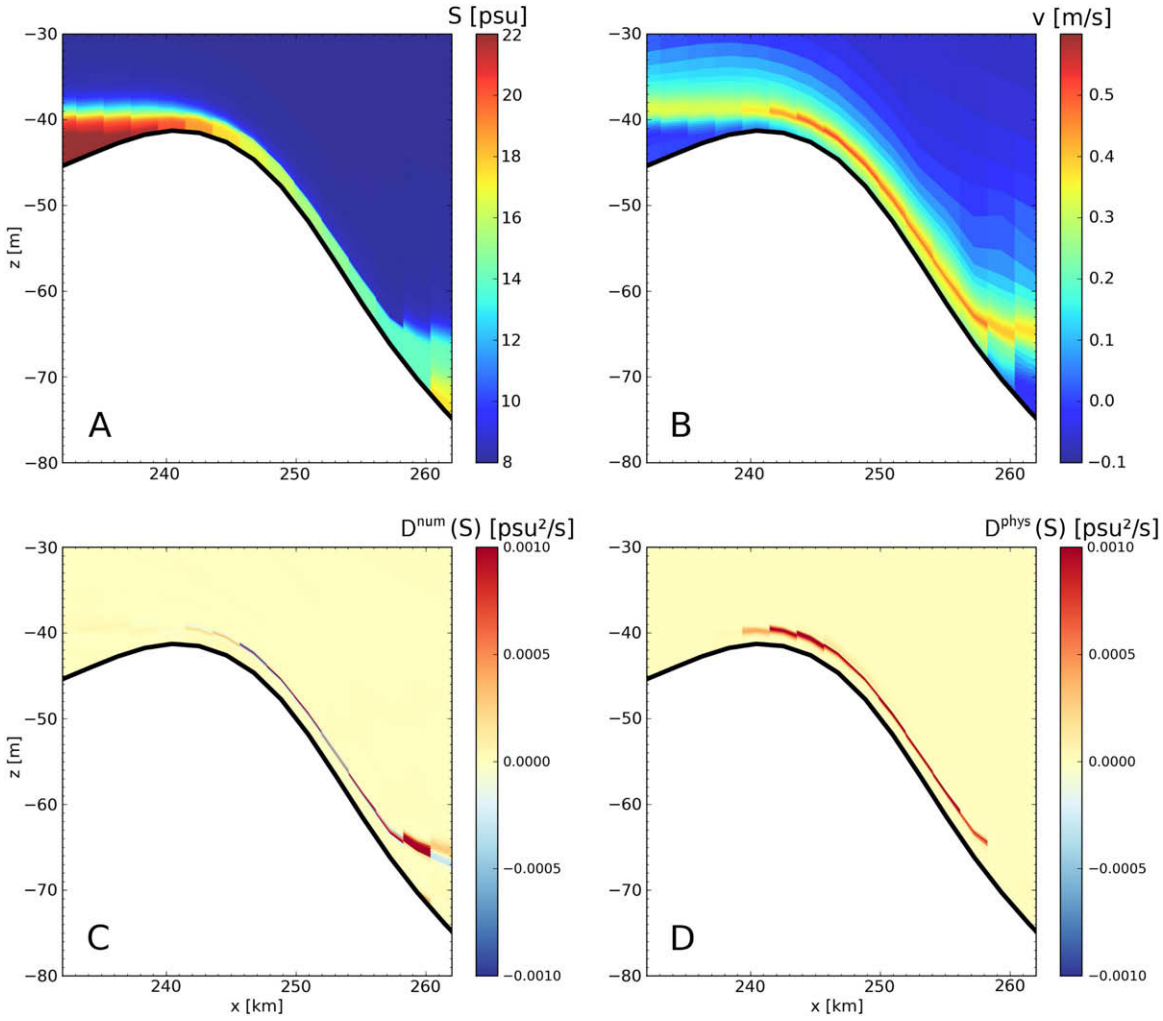

Fig. 5. As Fig. 4 but for the simulation with an adaptive vertical grid.

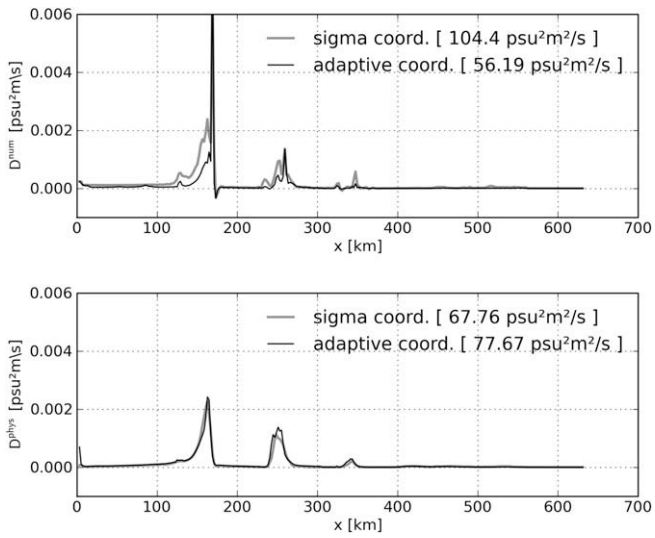

Fig. 6. Horizontal distribution of vertically integrated and temporally averaged numerical salinity variance decay in the upper panel and physical salinity variance decay in the lower panel. For a quantitative comparison, the spatially integrated and temporally averaged salinity variance decay is given as number in the legends.

The mean kinetic energy of the system

$$E_{kin} = \frac{1}{2V} \sum_{i,j,k} \left[\Delta V_{i,j,k} \left(u_{i,j,k}^2 + v_{i,j,k}^2 \right) \right] \tag{48}$$

is calculated as measure for the pressure gradient error, where $\Delta V_{i,j,k}$ are the grid cell volumes, where i,j,k denote the grid cell numbering in both horizontal and the vertical direction, $u_{i,j,k}$ and $v_{i,j,k}$ are the cell-mean velocities and V is the total volume of the domain. The evolution of the mean kinetic energy is then shown for 10 days of a full baroclinic simulation, as an indirect measure of the pressure gradient error. The simulation period is kept short in order to have only a small impact by other model techniques as the advection and turbulent mixing schemes. Besides, the grid adaption is expected to reduce the initial error in the pressure gradient calculation without having a direct influence on reducing the long-term envolving vorticity error.

Different vertical coordinate systems are applied to the system: A σ-grid, a s-grid with zooming to the surface and a set of adaptive grids. For the experiments the pressure gradient formulation (PGF) by Shchepetkin and McWilliams (2003) (labelled as ShMcW03 in the following) is applied, since it is widely used in the ocean modelling community. The sigma grid experiment is additionally set up with a standard Jacobian PGF (Mellor et al., 1994) in order to show differences due to an improved PGF.

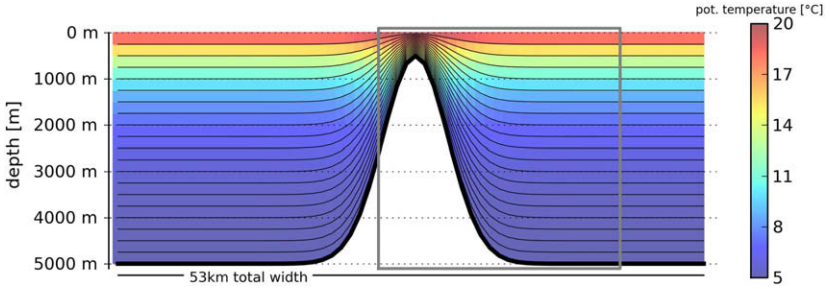

Fig. 7. The initial temperature distribution for the seamount experiment with 20 vertical σ-layers. The black lines denote the layer interfaces. In further plots, the part of the domain denoted by the gray box is shown.

For all the grid adaptions, the Lagrangian and isopycnal tendency are switched off, but filters for layer heights ($\alpha_{dif} = 0.2$) and interface positions ($\alpha_{hor} = 0.5$) are applied. Both filters allow for a smooth layer interface distribution. A strong filtering of interface positions is assumed to reduce the pressure gradient errors significantly, but will continuously lift the interface of the bottom layers around the seamount. Only a small amount of interface position filtering is applied to keep realistic vertical resolutions here. The Table 3 shows the parameters used for grid adaptions in the seamount experiments.

The adaptive grids are pre-adapted for the first 50 time steps, starting from a sigma grid, in order to avoid kinetic energy contributions due to an initial movement of the whole grid towards a balanced, initial layer distribution in terms of the adaption. The pre-adaption creates a balance of the impacts by the initial density profile and the bathymetry. The initial temperature profile is interpolated onto the model grid afterwards, as also done for the sigma and the zoomed, but fixed grid.

4.3.1. Classical setup

Fig. 8 shows the layer distribution for the different experiments. For the adaptive grids, the lower layers congregate at the top of the seamount and are released from the sea bed successively with depth as a result of the filter for interface positions. The evolution of kinetic energy in Fig. 9 shows a range of 3.5 orders of magnitude. The highest kinetic energy is found in the σ-coordinate system with the standard Jacobian PGF. A decrease of two orders of magnitude is obtained by using the ShMcW03 PGF. By applying a zooming towards the surface, the kinetic energy is decreased slightly again. The adaptive grids show a generally but only slightly higher kinetic energy than the σ-coordinate experiment with the same PGF, which is mainly related to the model reaction at the surface. The adaption to stratification needs a strong zooming towards the surface to keep resolution at the surface. The vertical optimisation is limited here because there are not enough layer interfaces close to the surface for the initial sigma grid. A good adaptive grid with even less kinetic energy after 10 days of simulation is created by just a zooming towards the surface and the horizontal filtering. The resolution is higher at the surface but still sufficient in the deeper parts of the ocean compared to the adaption to stratification. Compared to the fixed, zoomed grid, the filtering in the adjusted the layer interfaces horizontally, which turns out to be beneficial. In the classical setup, strong pressure gradient errors occur in the surface layer. Although the layer interfaces are not as steep as next to the seamount, the implied along-layer density gradient is strong, due to the exponential temperature profile. A strong vertical density gradient exists by definition in the surface layer, which is not resolved by the model grid.

Table 3
Parameters for the grid adaptions in the seamount experiments.

Adaption to	c_{N^2}	c_{S^2}	c_d	d_{surf} (m)	α_{hor}	α_{dif}
Only filtered interface position	0.0	0.0	0.0	200	0.2	0.5
Zooming to surface + filter	0.0	0.0	0.3	200	0.2	0.5
N^2 + filter	0.05	0.0	0.0	200	0.2	0.5
N^2 + zooming + filter	0.05	0.0	0.3	200	0.2	0.5
N^2 + strong zooming + filter	0.05	0.0	0.6	200	0.2	0.5

4.3.2. Mixed-layer setup

The standard seamount experiment showed that zoomed, but fixed grids have good performance without the grid adaption overhead, if the region of interest is located at the surface or the bottom. A second experiment with an expanded mixed layer will show the advantages of the grid adaption in such a scenario. The mixed layer is extended to the upper 450 m in the domain in the second experiment. The grid adaption will include now alignment of the grid layers with the thermocline, which cannot be achieved with a zooming to the surface only. Fig. 10 shows the same experiments as for the standard setup but with a mixed-layer initial temperature profile. Without including a zooming towards the surface for the adaptive grids, the mixed layer is resolved with very few grid layers only. This does not constrain the density profile by the layer distribution, but the grid is pathologic in terms of realistic ocean modelling, when air-sea interactions are expected.

In the temporal evolution of the kinetic energy in Fig. 11, higher kinetic energies can be found due to the pressure gradient error by sloping coordinates at the pycnocline. The advantage by zooming towards the surface is insignificant in terms of kinetic energy evolution for the fixed grids. The kinetic energies are still reduced by one order of magnitude with applying a higher-order pressure gradient scheme compared to the standard Jacobian scheme. By applying the grid adaption, a reduction of kinetic energy by again up to almost one order of magnitude can be found. The pure horizontal filtering again induces less kinetic energy than the fixed grids, but the adaption to stratification in addition with the zooming towards the surface is most beneficial here. In the scenario, where a pure zooming to the surface cannot improve the pressure gradient calculation, the adaptive vertical grids show an improvement compared to fixed grids, when adapting the coordinates to stratification. The horizontal filtering is then used as control on the regularity of the grid. Additionally, the resolution at the pycnocline is improved such that all the physical processes at the pycnocline will also benefit in realistic simulations.

4.4. Coastal upwelling

A last experiment shows the interaction of different processes and the performance of vertically adaptive coordinates in a full-physics scenario. The model domain is an infinitely long channel of parabolic shape and initialised with a horizontally homogeneous temperature stratification. Fig. 12 shows the temperature distribu-

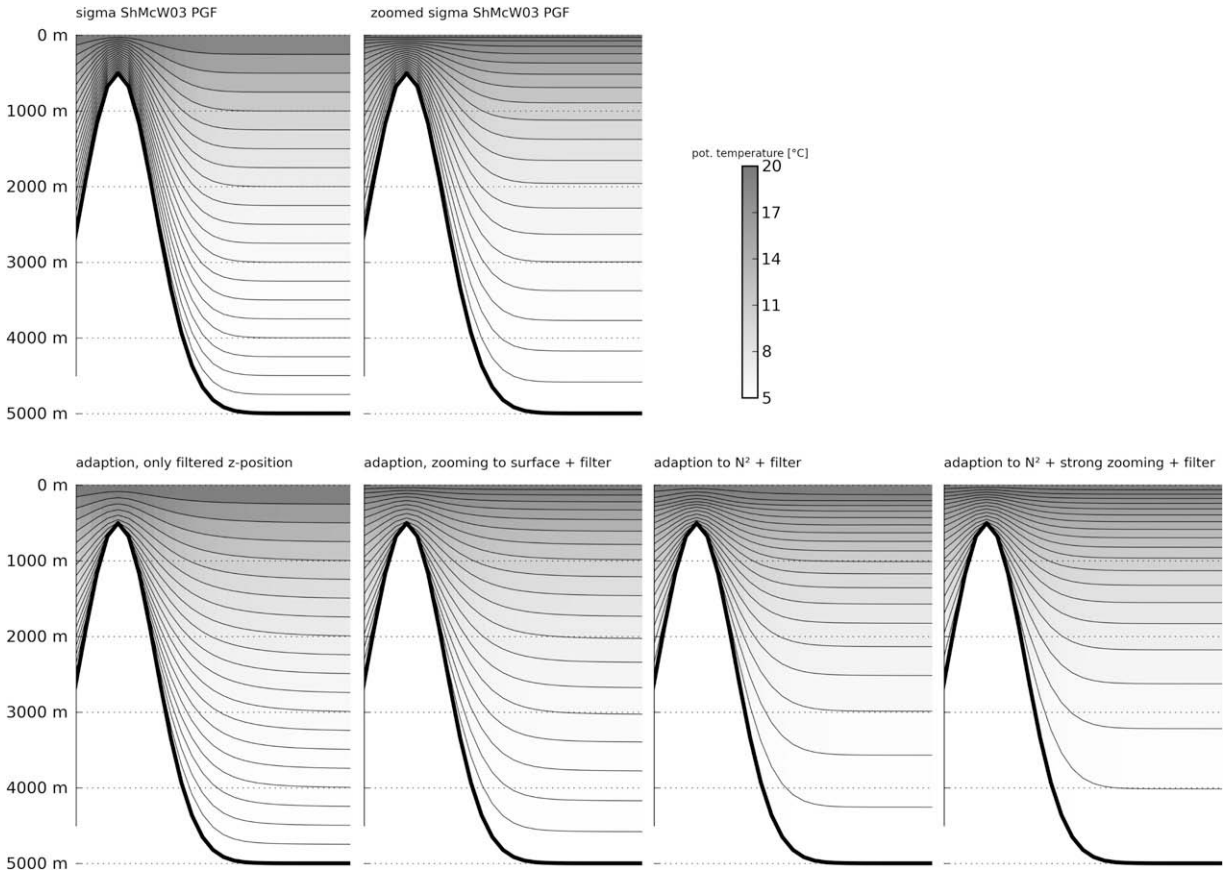

Fig. 8. The layer distribution (black lines) and the temperature (grayscale) for the different vertical discretisations in the classical seamount experiment.

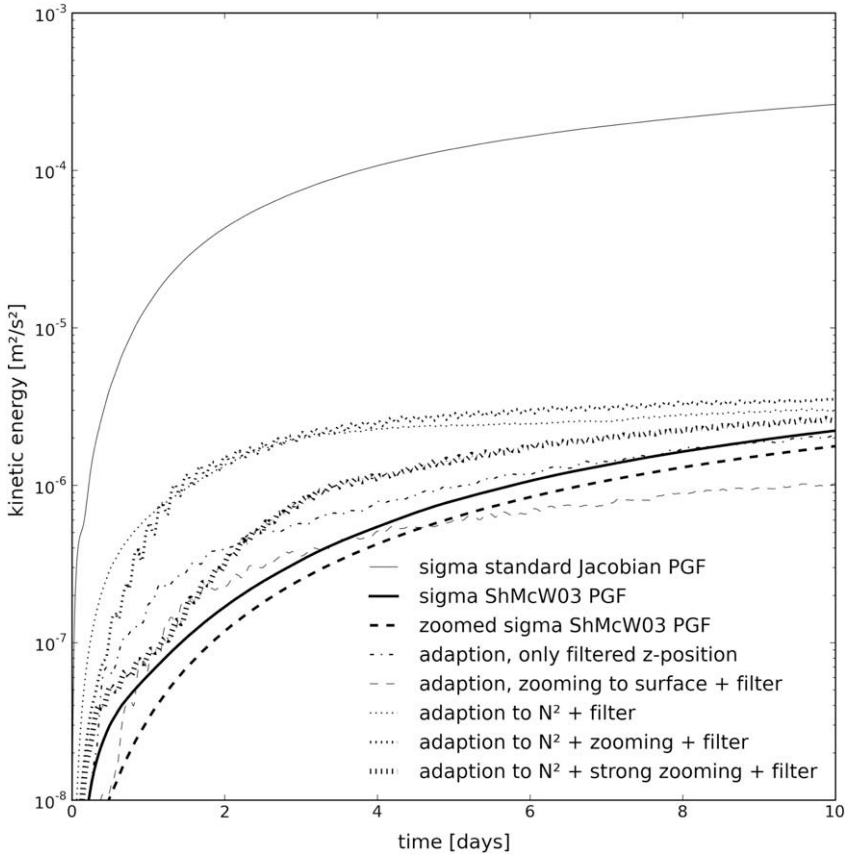

Fig. 9. The temporal evolution of mean kinetic energy for the different vertical discretisations in the classical seamount experiment.

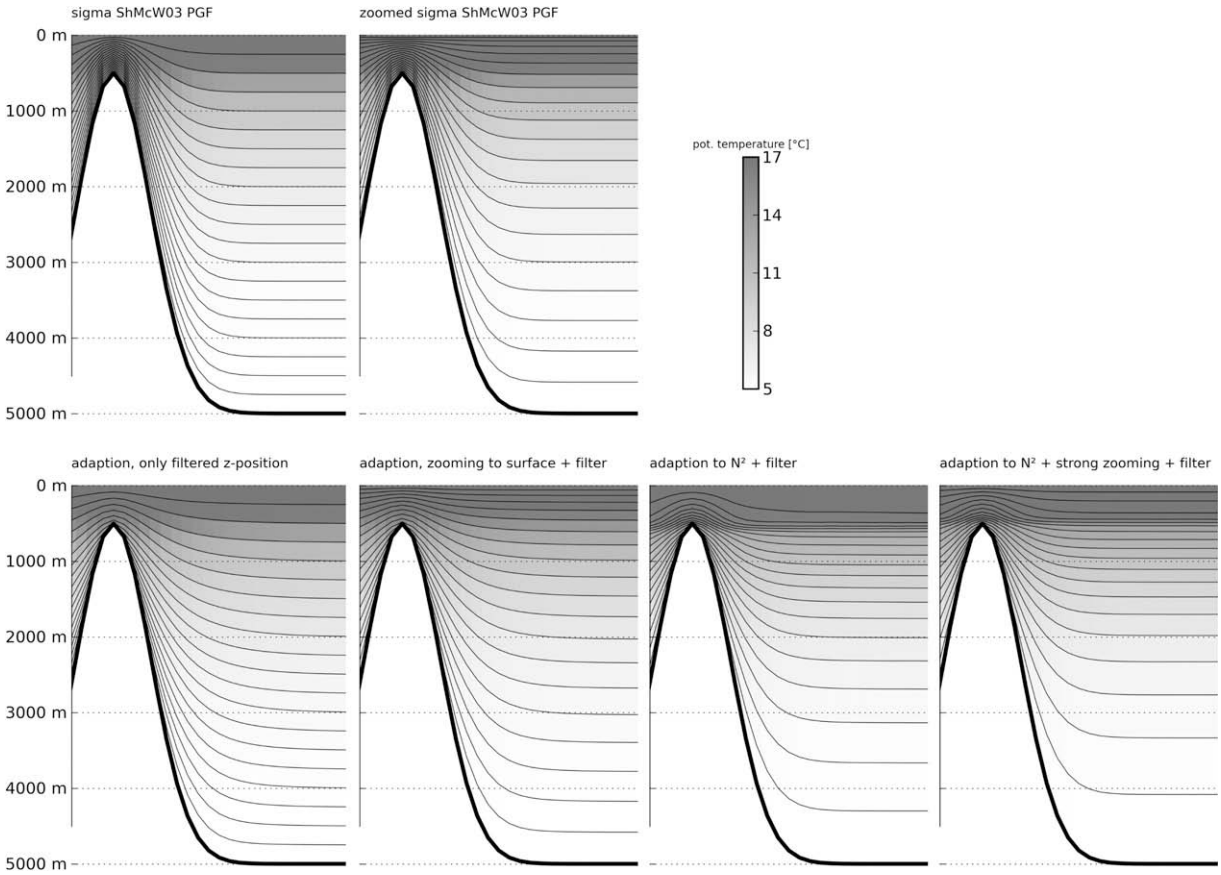

Fig. 10. The layer distribution (black lines) and the temperature (grayscale) for the different vertical discretisations in the extended mixed layer seamount experiment.

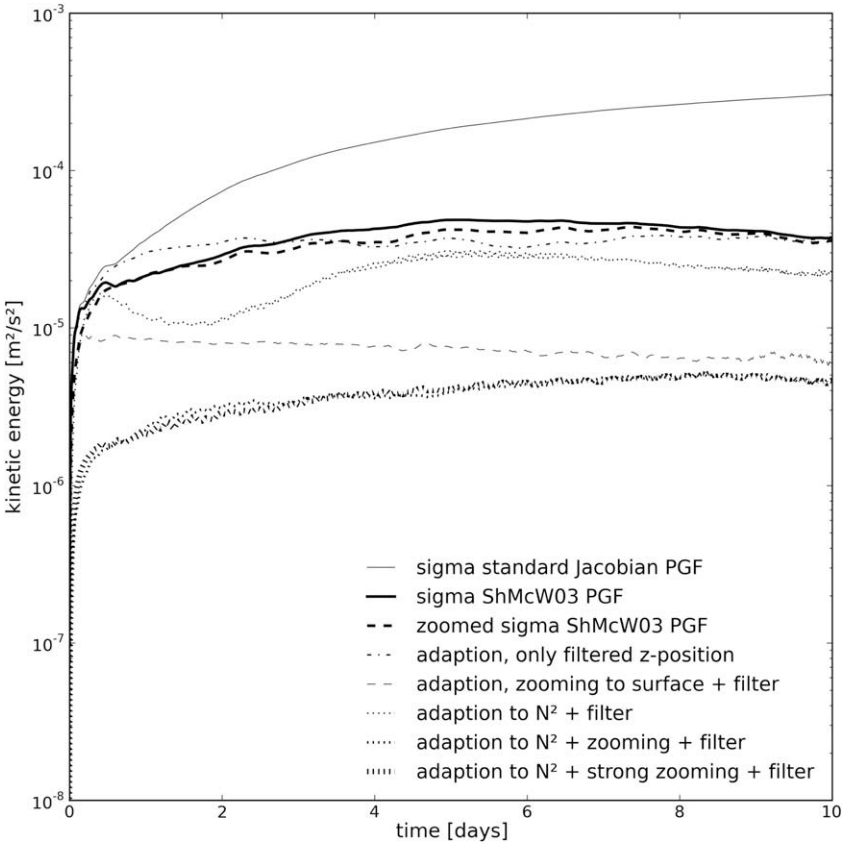

Fig. 11. The temporal evolution of mean kinetic energy for the different vertical discretisations in the extended mixed layer seamount experiment.

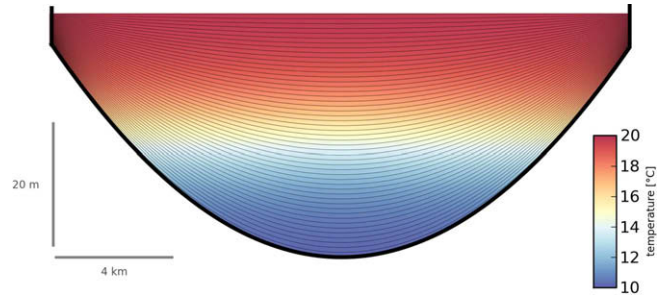

Fig. 12. Cross-channel slice in the coastal upwelling experiment, showing the initial temperature distribution for 50 σ-layers.

tion for a cross-channel slice. At a latitude of 55 °N, a wind stress of 0.2 Pa (constant in space and time) in along channel direction is applied at the surface, which causes upwelling at the left-hand side of the shown channel slice.

For having an infinite long channel, the model is configured to simulate a minimal set of two tracer and two velocity points in along-channel direction and periodic boundary conditions connecting the down- and up-stream side of the domain. The grid adaption is expected to resolve the temperature stratification well and follows the vertical displacement of the pycnocline. On the other hand, resolution should not be lost at the surface, when the wind-induced surface shear has to be resolved as long as the wind is active. The main goal is to increase the resolution at the pycnocline as well as at the surface such that the numerical mixing is reduced. In the adaptive grid mode, a pre-adaption of the layers to the initial condition of 50 iteration steps was applied. The three discussed adaptive grids are (A) adaptive to shear and stratification with a grid timescale of 1 h, (B) like (A), but with a grid timescale of 2 h (C) adaptive to shear only with a grid timescale of 2 h, with the parameters as listed in Table 4.

In Fig. 13, the mean numerical and physical tracer variance decay are shown for different vertical discretisations. The temperature distribution looks similar for the different vertical discretisations, so that the evaluation of the numerical mixing shows the real advantages regarding long integration periods for realistic simulations.

Most of the curves of the numerical mixing show a characteristic profile as denoted with (a)–(d) in Fig. 13. In addition, the vertical profiles of the temperature in the centre of the channel are shown with the cross-channel resolution in Fig. 15. The adaptive grid shows a very similar vertical profile, meaning the same physics, as the simulation with the fixed grid.:

(a) During the first 3 h, the currents due to the onset of wind are developing without generating strong across-channel flow near the bed. The numerical mixing remains weak in that period. The adaptive grids are further zooming towards a balanced state of grid adaption for the initial density distribution. The used third-order TVD scheme even enhances the gradients by numerical un-mixing with gaining resolution at the pycnocline. The anti-diffusive part of the advection scheme (depending on the choice of the limiter) is adding up to a global un-mixing for a short period at the beginning of the simulation. At the same time, numerical mixing started with the zooming of the layers towards the wind induced shear region near the surface. The integrated effect of the initial layer re-distribution is adding up back to zero after 3–4 h of simulation and can further be compared with the fixed grid simulations. Also Burchard and Rennau (2008) found that TVD schemes can increase the integrated tracer variance.

(b) When the cross-channel currents are developing due to rotation and the upwelling is starting, then the dense water is advected in along-layer direction in the near bed layers. This causes a huge amount of the overall numerical mixing and cannot be decreased by the usage of adaptive vertical grids.

Table 4
Parameters for the grid adaptions in the upwelling experiments.

Grid No.	α_{hor}	α_{lag}	α_{dif}	α_{iso}	c_{N^2}	c_{S^2}	c_d	d_{min} (m)	t_{grid} (h)
(A)	0.0	0.0	0.3	0.0	0.2	0.1	0.0	0.05	1
(B)	0.0	0.0	0.3	0.0	0.2	0.1	0.0	0.05	2
(C)	0.0	0.0	0.3	0.0	0.0	0.1	0.0	0.05	2

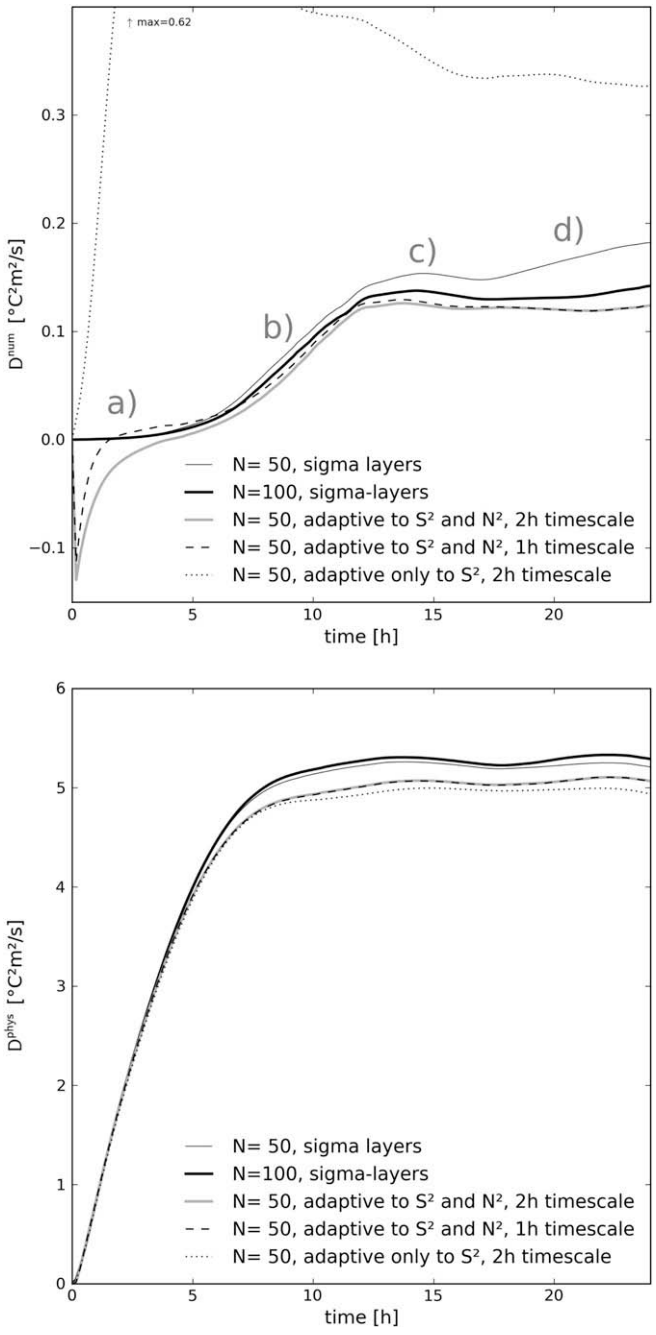

Fig. 13. The cross-sectionally integrated, numerical (upper panel) and physical (lower panel) tracer variance decay averaged over time for different vertical discretisations for the upwelling experiment. The labels (a)–(d) denote characteristic periods, which are discussed in the text.

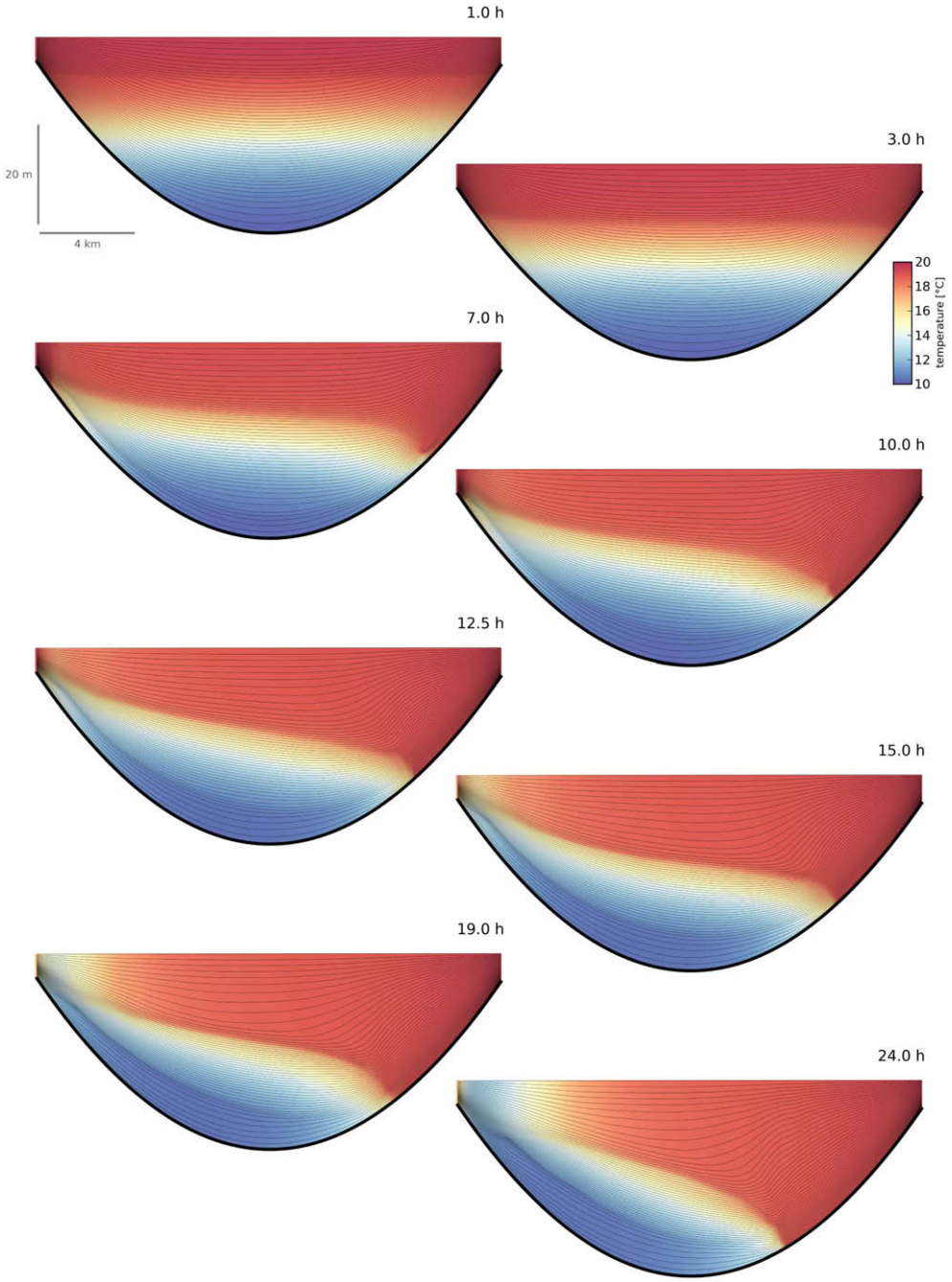

Fig. 14. Cross-channel slices in the coastal upwelling experiment, showing the temperature distribution for 50 vertical layers and the best grid adaption in terms of the numerical mixing.

(c) After 12 h, when geostrophical adjustment is almost established (note that the inertial period is 14.6 h), the upwelling builds an internal pressure gradient balancing the barotropic pressure gradient and mainly turbulent mixing takes place, see times 12.5 and 15 h in Fig. 14. The numerical mixing is very low during the physical mixing process, thus the temporal mean is decreased slightly.

(d) After 17 h, the mixing and re-circulation on the shallow, left-hand side of the channel reduces the internal pressure gradient and forces a further movement of dense water with strong vertical component. The numerical mixing increases again for the fixed grid, whereas the grid adaption follows the vertical movement and additional, significant numerical mixing is avoided. The double resolution, fixed grid also shows only a very small amount of additional numerical mixing.

The fixed grid in double vertical resolution reduces the mean numerical mixing for the shown period by 25%. With grid adaption at the lower vertical resolution, the numerical mixing is another 10% less than for the double vertical resolution. In Fig. 13, also the grid adaption to only current shear is shown partially. The resulting grid (not shown) looks promising, because the shear mostly occurs also at pycnoclines. But the grid adaption is moving the layer interfaces through the pycnocline at the beginning of the simulation, where only the surface shear is target of the vertical

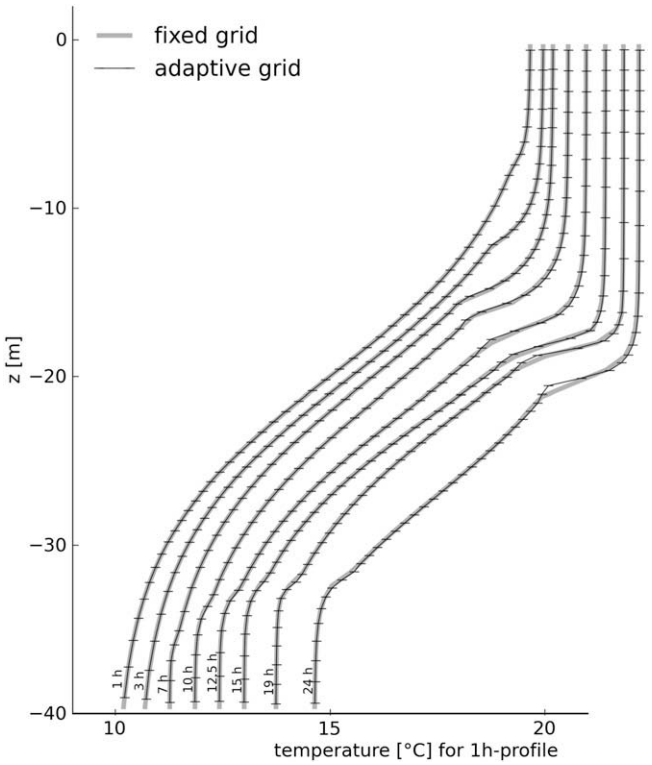

Fig. 15. The vertical temperature profile for the deepest point in the channel is shown for the adaptive and fixed grid together with two vertical lines denoting the vertical positions of tracer points in the water column. The temperature axis is valid for the 1 h profile, each further profile is shifted by 0.5 °C per profile.

grid adaption. The numerical mixing does not destroy the pycnocline completely in this case, but for realistic applications with a multiple on- and off-set of wind events, a background stratification might be mixed up for long integration periods.

Additionally to the numerical mixing, the mean physical mixing is evaluated for the different grids. All the curves show a similar evolution and are levelling out at about 97% of the overall mixing for the whole model domain. The differences due to the different vertical grids for the physical mixing are much higher than for the numerical mixing. Here, the model grid is determining the performance of the mixing scheme such that even less physical mixing is found for the adaptive grids. In spite of the lack of an analytical or observed solution, the result is still remarkable since the difference between the fixed and the adaptive grids grows when the density interface is displaced.

The coastal upwelling experiment shows the performance of the grid adaption in a full physics simulation. The integration time of 24 h is short, but the analysis of the numerical mixing shows that the grid adaption reduces the numerical mixing even more than the doubling of the vertical resolution. The simulated physical scenario is not changed significantly by the grid adaption, but the resolution at the pycnocline is higher than for the fixed grid and the grid is following the stratification. This supports a good representation of the physical processes in the model such as mixing in a stratified regime and advection along isopycnals.

5. Conclusions

A method for using non-uniform adaptive vertical grids is presented here. It is easy to implement the technique into other ocean models than GETM, even for models with unstructured grids. In the latter case, it should be possible to combine horizontal and vertical grid adaption. All other model techniques such as advection, pressure gradient or turbulence closure schemes are not affected by the grid method. The computational overhead is 30–40% in average as calculated from model run time and refers to a compilation with standard optimisation settings running on a standard Linux PC. This is computationally less expensive than doubling vertical resolution of fixed coordinates and still reduces numerical discretisation errors more effectively.

It is shown that adaptive vertical grids are reducing the numerical mixing substantially for a set of idealised examples with respect to know problems in ocean modelling such as internal seiching in stratified basins or dense overflows. The physically-motivated tracer mixing in the model can be enhanced by a reduced numerical tracer variance decay. Generally, the numerical mixing is reducing the performance of the turbulent mixing schemes, which have been carefully calibrated by means of theoretical considerations, and field and laboratory data.

Further, one example shows that the pressure gradient error can be considerably reduced by the adaptive grid method. There is evidence that these benefits will reduce uncertainties in model results of stratified seas, which has to be shown for realistic cases in the future.

The optimal parameters controlling the grid adaption are varying depending on the scenario in the experiments shown here. This is due to the different horizontal and temporal scales in the experiments. It turns out to be beneficial to use mainly the grid adaption to stratification and the horizontal filter of grid layer heights. In dynamically active cases, a shorter timescale and Lagrangian tendency for the grid adaption are additionally advantageous in order to decrease the numerical mixing.

The parameter space for improvements of model results needs to be further explored by carrying out tests in realistic applications. The potential of the adaptive grid method is to provide new ways to improve model results for simulations where fixed (bottom-fitted) coordinates give only insufficient results. Umlauf et al. (submitted for publication) applied the presented grid adaption method presented here to strongly stratified shear flow in order to approach isopycnal coordinates in these parts of the model domain. There, non-isopycnally aligned coordinates give intolerable discretisation errors due to an aliasing between isopycnals and grid lines. For simulations with long integration periods, reduced numerical mixing due to adaptive grids helps to preserve the stratification near steep slopes.

The modeller's knowledge of the expected regimes in the simulation can be used for controlling the grid adaption. A changing regime such as a seasonally moving thermocline or substantial tracer variation due to fluxes through open boundaries results in a dynamical re-distribution of the grid towards the specified optimisation of the vertical resolution.

Acknowledgements

The work of Richard Hofmeister is funded by the DFG (German Research Foundation) through the project QuantAS-Nat. The work by Hans Burchard has been supported by the Alexander-von-Humboldt Prize 2001/2002 awarded by the Belgian National Fund for Scientific Research (FNRS).

References

Adcroft, A., Hallberg, R., 2006. On methods for solving the oceanic equations of motion in generalized vertical coordinates. Ocean Modell. 11, 224–233.

Arneborg, L., Fiekas, V., Umlauf, L., Burchard, H., 2007. Gravity current dynamics and entrainment – a process study based on observations in the Arkona Basin. J. Phys. Oceanogr. 37, 2094–2113.

Auclair, F., Marsaleix, P., Estournel, C., 2000. Sigma coordinate pressure gradient errors: evaluation and reduction by an inverse method. J. Atmos. Oceanic Technol. 17, 1348–1367.

Banas, N.S., Hickey, B.M., 2005. Mapping exchange and residence time in a model of Willapa Bay, Washington, a branching, microtidal estuary. J. Geophys. Res. 110, C11011. doi:10.1029/2005JC002950.

Beckers, J.-M., Burchard, H., Deleersnijder, E., Mathieu, P.-P., 2000. Numerical discretisation of rotated diffusion operators in ocean models. Mon. Weather Rev. 128, 2711–2733.

Beckmann, A., Döscher, R., 1997. A method for improved representation of dense water spreading over topography in geopotential-coordinate models. J. Phys. Oceanogr. 27, 581–591.

Beckmann, A., Haidvogel, D.B., 1993. Numerical simulation of flow around a tall isolated seamount. Part I: problem formulation and model accurancy. J. Phys. Oceanogr. 23, 1736–1753.

Behrens, J., Dethloff, K., Hiller, W., Rinke, A., 2000. Evolution of small-scale filaments in an adaptive advection model for idealized tracer transport. Mon. Weather Rev. 128, 2976–2982.

Blayo, E., Debreu, L., 1999. Adaptive mesh refinement for finite-difference ocean models: first experiments. J. Phys. Oceanogr. 29, 1239–1250.

Bleck, R., 2002. An oceanic general circulation model framed in hybrid isopycnic-cartesian coordinates. Ocean Modell. 4, 55–88.

Bleck, R., Smith, L.T., 1990. A wind-driven isopycnic coordinate model of the North and Equatorial Atlantic Ocean. 1. Model development and supporting experiments. J. Geophys. Res. 95, 3273–3285.

Blumberg, A.F., Mellor, G.L., 1987. A description of a three dimensional coastal ocean model. In: Heaps, N. (Ed.), Three Dimensional Shelf Models. Coastal Estuarine Science, vol. 5. AGU, Washington, DC, pp. 1–16.

Bryan, K., 1969. A numerical method for the study of the circulation of the world ocean. J. Comput. Phys. 4, 347–376.

Burchard, H., Beckers, J.-M., 2004. Non-uniform adaptive vertical grids in one-dimensional numerical ocean models. Ocean Modell. 6, 51–81.

Burchard, H., Bolding, K., 2002. GETM – a general estuarine transport model. Scientific documentation. Tech. Rep. EUR 20253 EN, European Commission.

Burchard, H., Bolding, K., Rippeth, T.P., Stips, A., Simpson, J.H., Sündermann, J., 2002. Microstructure of turbulence in the Northern North Sea: a comparative study of observations and model simulations. J. Sea Res. 47, 223–238.

Burchard, H., Bolding, K., Villarreal, M.R., 2004. Three-dimensional modelling of estuarine turbidity maxima in a tidal estuary. Ocean Dyn. 54, 250–265.

Burchard, H., Flöser, G., Staneva, J.V., Riethmüller, R., Badewien, T., 2008. Impact of density gradients on net sediment transport into the Wadden Sea. J. Phys. Oceanogr. 38, 566–587.

Burchard, H., Janssen, F., Bolding, K., Umlauf, L., Rennau, H., 2009. Model simulations of dense bottom currents in the Western Baltic Sea. Cont. Shelf Res. 29, 205–220.

Burchard, H., Petersen, O., 1997. Hybridisation between σ and z coordinates for improving the internal pressure gradient calculation in marine models with steep bottom slopes. Int. J. Numer. Meth. Fluids 25, 1003–1023.

Burchard, H., Rennau, H., 2008. Comparative quantification of physically and numerically induced mixing in ocean models. Ocean Modell. 20, 293–311.

Chassignet, E.P., Hurlburt, H.E., Smedstad, O.M., Halliwell, G.R., Wallcraft, A.J., Metzger, E.J., Blanton, B.O., Lozano, C., Rao, D.B., Hogan, P.J., Srinivasan, A., 2006. Generalized vertical coordinates for eddy-resolving global and coastal ocean forecasts. Oceanography 19, 20–31.

Chu, P.C., Fan, C., 1997. Sixth-order difference scheme for sigma coordinate ocean models. J. Phys. Oceanogr. 27, 2064–2071.

Deleersnijder, E., Ruddick, K.G., 1992. A generalized vertical coordinate for 3D marine problems. Bull. Soc. Roy. Sci. Liège 61, 489–502.

Dewar, W., McDougall, T., 2000. The numerical solution of the one-dimensional advection-diffusion equation in layered coordinates. Mon. Weather Rev. 128, 2575–2587.

Ezer, T., 2005. Entrainment, diapycnal mixing and transport in three-dimensional bottom gravity current simulations using the Mellor–Yamada turbulence scheme. Ocean Modell. 9, 151–168.

Feistel, R., Nausch, G., Hagen, E., 2006. Unusual Baltic inflow activity 2002/3 and varying deep-water properties. Oceanologia 48, 21–35.

Fiedler, B., 2002. Grid adaptation and its effect on entrainment in an E-l model of the atmospheric boundary layer. Mon. Weather Rev. 130, 733–740.

Gent, P.R., McWilliams, J.C., 1990. Isopycnal mixing in ocean circulation models. J. Phys. Oceanogr. 20, 150–155.

Griffies, S., Böning, C., Bryan, F., Chassignet, E., Gerdes, R., Hasumi, H., Hirst, A., Treguier, A.-M., Webb, D., 2000. Developments in ocean climate modeling world climate research programme/world ocean circulation experiment working group on ocean model development. Ocean Modell. 2, 123–192.

Halliwell, G.R., 2004. Evaluation of vertical coordinate and vertical mixing algorithms in the hybrid-coordinate ocean model (hycom). Ocean Modell. 7, 285–322.

Haney, R.L., 1991. On the pressure gradient force over steep topography in sigma coordinate ocean models. J. Phys. Oceanogr. 21, 610–619.

Hofmeister, R., Burchard, H., Bolding, K., 2009. Realistic modelling of stratification in the Limfjord. Cont. Shelf Res. 29 (11–12), 1515–1524.

Holt, J., James, I., 2001. An s coordinate density evolving model of the northwest european continental shelf-1, model description and density structure. J. Geophys. Res. 106, 14015–14034.

Ilicak, M., Özgökmen, T.M., Peters, H., Baumert, H., Iskandarani, M., 2008. Performance of two-equation turbulence closures in three-dimensional simulations of the Red Sea overflow. Ocean Modell. 24, 122–139.

Iselin, J., Prusa, J., Gutowski, W., 2002. Dynamic grid adaptation using the MPDATA scheme. Mon. Weather Rev. 130, 1026–1039.

Kasahara, A., 1974. Various vertical coordinate systems used for numerical weather predictions. Mon. Weather Rev. 102, 509–522.

Lander, J.W.M., Blokland, P.A., de Kok, J.M., 1994. The three-dimensional shallow water model TRIWAQ with a flexible vertical grid definition. Tech. Rep. RIKZ/OS-96.104x, SIMONA report 96-01. National Institute for Coastal and Marine Management/RIKZ, The Hague, The Netherlands.

LeBlond, P.H., Mysak, L., 1978. Waves in the Ocean. Elsevier, New York. 602 pp.

Liseikin, V., 1999. Grid Generation Methods. Springer, Berlin-Heidelberg.

Madec, G., Delecluse, P., Imbard, M., Levy, C., 1998. Opa 8.1 Ocean General Circulation Model Reference Manual. Note du Pole de modélisation, vol. 11. Institut Pierre-Simon Laplace (IPSL), France, pp. 1–91.

Marchesiello, P., Debreu, L., Couvelard, X., 2009. Spurious diapycnal mixing in terrain-following coordinate models: the problem and a solution. Ocean Modell. 26, 156–169.

Mellor, G., Blumberg, A., 1985. Modeling vertical and horizontal diffusivities with the sigma coordinate system. Mon. Weather Rev. 113, 1379–1383.

Mellor, G.L., Ezer, T., Oey, L.-Y., 1994. The pressure gradient conundrum of sigma coordinate ocean models. J. Atmos. Oceanic Technol. 11, 1126–1134.

Mellor, G.L., Oey, L.-Y., Ezer, T., 1998. Sigma coordinate pressure gradient errors and the seamount problem. J. Atmos. Oceanic Technol. 15, 1122–1131.

Peters, H., Baumert, H., 2007. Validating a turbulence closure against estuarine microstructure measurements. Ocean Modell. 19, 183–203.

Pietrzak, J., 1998. The use of TVD limiters for forward-in-time upstream-biased advection schemes in ocean modeling. Mon. Weather Rev. 126, 812–830.

Pietrzak, J., Jakobson, J., Burchard, H., Vested, H.-J., Petersen, O., 2002. A three-dimensional hydrostatic model for coastal and ocean modelling using a generalised topography following co-ordinate system. Ocean Modell. 4, 173–205.

Rennau, H., Burchard, H., 2009. Quantitative analysis of numerically induced mixing in a coastal model application. Ocean Dyn. 59, 671–687.

Riemenscheider, U., Legg, S., 2007. Regional simulations of the Faroe Bank Channel overflow in a level model. Ocean Modell. 17, 93–122.

Shchepetkin, A.F., McWilliams, J.C., 2003. A method for computing horizontal pressure-gradient force in an oceanic model with a nonaligned vertical coordinate. J. Geophys. Res. 108. doi:10.1029/2001JC001047.

Simpson, J.H., Burchard, H., Fisher, N.R., Rippeth, T.P., 2002. The semi-diurnal cycle of dissipation in a ROFI: model-measurement comparisons. Cont. Shelf Res. 22, 1615–1628.

Skamarock, W., 1989. Truncation error estimates for refinement criteria in nested and adaptive models. Mon. Weather Rev. 117, 872–886.

Song, Y., Haidvogel, D.B., 1994. A semi-implicit ocean circulation model using a generalised topography-following coordinate. J. Computat. Phys. 115, 228–244.

Song, Y.T., 1998. A general pressure gradient formulation for ocean models. Part I: scheme design and diagnostic analysis. Mon. Weather Rev. 126, 3213–3230.

Song, Y.T., Hou, T., 2006. Parametric vertical coordinate formulation for multiscale, Boussinesq, and non-Boussinesq ocean modeling. Ocean Modell. 11 (3–4), 298–332.

Song, Y.T., Wright, D.G., 1998. A general pressure gradient formulation for ocean models. Part II: energy, momentum and bottom torque consistency. Mon. Weather Rev. 126, 3231–3247.

Souza, A.J., Fisher, N.R., Simpson, J.H., Howarth, M.J., 2008. Effects of tidal straining on the semi-diurnal cycle of dissipation in the Rhine region of freshwater influence: comparison of model and measurements. J. Geophys. Res. 113, C01011. doi:10.1029/2006JC004002.

Stanev, E., Beckers, J.-M., 1999. Barotropic and baroclinic oscillations in strongly stratified ocean basins. Numerical study of the Black Sea. J. Mar. Syst. 19, 65–112.

Stanev, E.V., Wolff, J.-O., Burchard, H., Bolding, K., Flöser, G., 2003. On the circulation in the East Frisian Wadden Sea: numerical modelling and data analysis. Ocean Dyn. 53, 27–51.

Staneva, J., Stanev, E.V., Wolff, J.-O., Badewien, T.H., Reuter, R., Flemming, B., Bartholomä, A., Bolding, K., 2009. Hydrodynamics and sediment dynamics in the German Bight. A focus on observations and numerical modelling in the East Frisian Wadden Sea. Cont. Shelf Res. 29, 302–319.

Stelling, G.S., Van Kester, T., 1994. On the approximation of horizontal gradients is σ co-ordinates for bathymetry with steep bottom slopes. Int. J. Numer. Meth. Fluids 18, 915–935.

Thompson, J., Warsi, Z., Mastin, C., 1985. Numerical Grid Generation – Foundations and Applications. Elsevier, New York.

Umlauf, L., Arneborg, L., Hofmeister, R., Burchard, H., submitted for publication. Entrainment in shallow rotating gravity currents: a modeling study. J. Phys. Oceanogr.

Umlauf, L., Burchard, H., 2005. Second-order turbulence models for geophysical boundary layers. A review of recent work. Cont. Shelf Res. 25, 795–827.

Umlauf, L., Burchard, H., Bolding, K., 2005. General Ocean Turbulence Model. Source code documentation. Tech. Rep. 63. Baltic Sea Research Institute Warnemünde, Warnemünde, Germany.

Umlauf, L., Lemmin, U., 2005. Inter-basin exchange and mixing in the hypolimnion of a large lake: the role of long internal waves. Limnol. Oceanogr. 50, 1601–1611.

Wai, O.W.H., Lu, Q., 1999. Gradient-Adaptive-Sigma (GAS) grid for 3D mass-transport modeling. J. Hydraul. Eng. 125 (2), 141–151.

White, L., Adcroft, A., 2008. A high-order finite volume remapping scheme for nonuniform grids: the piecewise quartic method (PQM). J. Comput. Phys. 227, 7394–7422.